Title
HIGH RESOLUTION ELECTRON IMAGING: AN APPROACH TO THE ATOMIC CHARACTERIZATION OF MATERIALS

Author
Gronsky, R.

Publication Date
1978-03-01

To be published as a Chapter in "Electron and Positron Spectroscopy in Material Science and Engineering", Otto Buck, ed., Academic Press

HIGH RESOLUTION ELECTRON IMAGING: AN APPROACH TO THE ATOMIC CHARACTERIZATION OF MATERIALS

R. Gronsky, D. R. Clarke, and G. Thomas

March 1978

Prepared for the U. S. Department of Energy under Contract W-7405-ENG-48

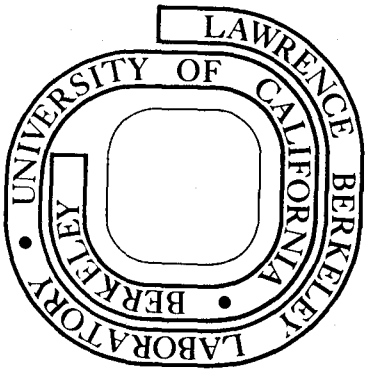

DISCLAIMER

HIGH RESOLUTION ELECTRON IMAGING:

AN APPROACH TO THE ATOMIC CHARACTERIZATION OF MATERIALS

R. Gronsky, D. R. Clarke* and G. Thomas

Materials and Molecular Research Division

Lawrence Berkeley Laboratory and Department of Materials

Science and Mineral Engineering,

University of California, Berkeley, California 94720

*Present address: Science Center, Rockwell International

1049 Camino Dos Rios, P. O. Box 1085

Thousand Oaks, California 91360

OUTLINE

HIGH RESOLUTION ELECTRON IMAGING: AN APPROACH TO THE ATOMIC CHARACTERIZATION OF MATERIALS

R. Gronsky, D. R. Clarke* and G. Thomas

Materials and Molecular Research Division

Lawrence Berkeley Laboratory and Department of Materials Science and Mineral Engineering,

University of California, Berkeley, California 94720

*Present address: Science Center, Rockwell International

1049 Camino Dos Rios, P. O. Box 1085

Thousand Oaks, California 91360

ABSTRACT

High resolution transmission electron microscopy directly provides an image of the spatial distribution of diffraction species within a material. This capability extends real space metallurgical analysis to the level of atomic dimensions and can be used to obtain both structural and chemical information about solid state phase transformations. In the present article, emphasis is placed on the study of grain boundaries in both metallic and ceramic alloys. Composition profiles within $\lesssim 10\text{Å}$ of the boundary plane have been detected indicating solute enrichment and the genesis of precipitation reactions. Microledges of one to two atomic layers in height have been imaged at interphase interfaces and the presence of amorphous layers at grain boundaries in commercial

ceramic systems has been verified. A review is given of the methods employed in high resolution electron imaging and the necessary developments for interpretable near-atomic resolution in close-packed materials are indicated.

I. INTRODUCTION

The interaction between a specimen and a beam of radiation can, with suitable control over experimental conditions, provide a variety of details about the atomic nature of matter. Fortunately when the illumination probe is a beam of electrons, the radiation which is scattered by, or emitted from, a specimen may either be analyzed with respect to its energy dispersion (spectroscopy) or focused to form an image (microscopy). As a result, electron spectroscopy and microscopy have evolved as complementary techniques in materials science. The fact that they can both be performed within a single instrument, the transmission electron microscope (TEM), has further promoted their tandem application to a wide range of metallic and ceramic alloys.

In this paper particular emphasis will be placed on the information obtained from elastically scattered electrons, viz. high resolution imaging and diffraction. Conventional methods of spectroscopic analyses in the TEM (X-ray microanalysis by STEM, energy loss spectroscopy) will not be discussed, but it will be shown how chemical information can be obtained (indirectly) from lattice parameter measurements of fringe spacings, plane by plane, i.e., to $< 2\mathring{A}$ spatial resolution.

In its own right the technique of transmission electron microscopy has undergone astounding development in recent years and for this reason it is being considered separately during the present symposium. Because

of the unequalled precision of modern electron optics, it is now possible to obtain a representation of the internal structure of a specimen which contains more than routine morphological information and in fact approaches the level of atomic resolution. With proper application of the technique, highly detailed structural as well as compositional information can be extracted on an extremely localized scale, even from materials of commercial interest.

In the present paper, a brief instructional summary will be given of the methods employed in high resolution electron imaging. A survey will also be made of those recent applications of the technique which have led to fundamental breakthroughs in current understanding of metallurgical and ceramic systems. In this area, particular emphasis will be placed on an example of intensive interest to spectroscopists and microscopists alike: the study of internal boundaries within crystalline materials. Finally an assessment will be made of the future directions for high resolution studies in materials science.

II. DESCRIPTION OF TECHNIQUE

A. Background

Conventional image formation in the TEM is achieved by magnifying either the transmitted beam, to form a bright field (BF) image, or one of the diffracted beams, to form a dark field (DF) image. The machanisms responsible for contrast under these conditions have been understood and utilized for quite some time (Thomas, 1962; Heidenreich, 1964; Hirsch et al., 1965). Nevertheless single beam imaging offers relatively little information about the fine structure of a specimen due to its highly restricted sampling of reciprocal space.

According to Abbé's theory (Born and Wolf, 1975), the complete diffraction pattern appearing at the back focal plane of an objective lens is actually a mapping of the Fourier transform of the specimen. Maximum information about the specimen should therefore be obtained by allowing all of these beams to interfere and form an image, i.e., another Fourier transform. Unfortunately this process is only possible for a perfect objective lens of infinite aperture. Real electron optical systems introduce modifications in both amplitude, due to a finite aperture size, and phase, due to lens aberrations, of the intensity distributions at the back focal plane (Cowley, 1975).

The phase distortion of a beam located at $\underset{\sim}{g}$ from the optic axis is described by a function (Misell, 1973),

$$\chi(g) = \frac{2\pi}{\lambda}\left(C_s \frac{\lambda^4 g^4}{4} - \Delta z \frac{\lambda^2 g^2}{2}\right) \qquad \text{Eq. (1)}$$

where C_s is the spherical aberration coefficient and Δz the extent of defocus of the objective for an electron wavelength, λ. Note that it is possible to some extent to lessen the effects of spherical aberration by adjusting the focus setting of the objective lens (Scherzer, 1949). In general the information contained within a particular beam g_1 will be faithfully transferred to the image only when its corresponding phase factor, $\exp(i\,\chi(g_1))$, is near unity. For this reason the variation of $\exp(i\,\chi(g))$ over all reciprocal space, known as the contrast transfer function (CTF), gives an indication of the imaging capabilities of an objective lens.

With most electron-optical systems currently in use, the transfer of high spatial frequencies poses considerable problems. The reason for this is the rapid oscillatory fluctuation of the CTF at large values of $\underset{\sim}{g}$ (small interatomic spacings). As a result it is very

difficult to resolve fine structures below 3,5Å point-to-point separation, and even if such detail is resolved, its relationship to the actual atomic arrangements within the specimen cannot be interpreted in any straightforward way.

B. Procedures

In spite of these limitations, when viewing crystals with large unit cells it is still possible to retain on the order of 100 beams within the objective aperture and produce correspondingly detailed "structural images" (Cowley and Iijima, 1972; Allpress and Sanders, 1973). The extent to which these images actually represent specimen structure is determined on the basis of image computations using the dynamical theory of electron scattering (Skarnulis, et al., 1976). Agreement between experiment and theory in these studies has been excellent and has fostered confidence in the interpretation and extended application of structural imaging (Bursill and Wilson, 1977).

Unfortunately these limitations are most restrictive in the case of nearly all commercially important materials, i.e., close-packed ceramic and metallic alloys. Consequently it is rarely possible to form a lattice image of these specimens using any higher than first order reflections, and usually no more than two beams at a time. The resulting images consist of a set(s) of fringes normal to the operating diffraction rector(s) which represent a particular set of atomic planes.

The most popular method (Dowell, 1963) of lattice fringe imaging incorporates two beams which, by changing the angle of illumination, are made to travel symmetrically with respect to the optic axis (Fig. 1). <Fig. 1> By this procedure, the magnitude of the phase distortion function (Eq. (1)) for the transmitted beam (0) located at -g/2 from the optic

axis is made equal to that for the diffracted beam (g) located at +g/2 from the optic axis. Therefore neither spherical aberration nor extent of defocus affects the in-focus image. This is an extremely useful characteristic of the "tilted illumination" technique which has enabled fringes of less than 1Å spacing to be resolved (Sieber and Tonar, 1975) and currently offers the best chances of success for detailed images of close-packed structures.

In practice lattice imaging generally requires thin specimens which have been oriented in a strong ($\underset{\sim}{s}$ = 0) Bragg condition for the imaging beams. These beams are symmetrically positioned with respect to the optic axis and surrounded by an objective aperture. All focusing and astigmatism corrections must then be made at high magnification on the area of interest. Finally the image is often recorded using a through-focus series on photographic film. For convenience of operation the microscope should be equipped with a high brightness source, high efficiency screen phosphor and/or image intensifier, and high vacuum. Once an image has been successfully produced, additional instrumentation, e.g., a microdensitiometer or optical diffractometer (Gronsky, et al., 1976) may also prove helpful in image analysis. Examples of the utilization of each of these methods are described in the following sections.

III APPLICATIONS

A. Structural Information at Atomic Plane Resolution

Many of the early studies utilizing lattice imaging for quantitative analysis of metallurgical problems involved crystal lattice dislocations (Komoda, 1966; Parsons and Hoelke, 1969; Phillips and Hugo, 1970). In these investigations, measurements were made of spacing perturbations surrounding terminating fringes and were related through isotropic

elasticity theory to the core width, core strain and long range matrix strains associated with dislocations. Such studies were also applied to crossed lattice images (Parsons and Hoelke, 1970) to examine the effects of lattice strain on atomic positions. However it was later demonstrated (Cockayne, et al., 1971), both experimentally and through contrast calculations, that an inclined lattice dislocation may produce either one or three terminating fringes in a two beam image, depending upon the direction ($+\underset{\sim}{g}$ or $-\underset{\sim}{g}$) of the operating reflection, Only when the dislocation line was oriented end-on with respect to the electron beam was a single fringe termination produced. These results demonstrated that extreme care must be taken to assure a one-to-one correspondence between terminating fringe profiles and matrix dislocations.

Subsequent research on dislocation strain fields was carried out using specimens prepared under rigid geometrical constraints (Phillips and Wagner, 1973) in order to assure the required end-on dislocation configuration. In other defect studies, Phillips (1972) successfully used lattice imaging to reveal microtwins of 3 atom plane thicknesses in silicon, as well as the occurrence of highly regular periodic structures in incoherent twin boundaries. It was also observed (Parsons, et al., 1970) that in ion-bombarded Ge, damaged regions exhibited no fringe contrast suggesting a lack of crystallinity, while similar defects in Cu were found to have a complex strain field detected only in the lattice image mode (Howe and Rainville, 1972).

By providing detail which supersedes the resolution capabilities of other experimental techniques, lattice imaging has considerably enhanced the characterization of phase transformation behavior. Following the direct observation (Parsons et al., 1970) of G.P. zones in Al-Cu by this method, a quantitative assessment of zone size, density and displacement

field was subsequently performed at the atomic level (Pillips, 1973) and more recently extended through the precipitation sequence (Phillips, 1975). This latter study revealed a continuous structure progression from G.P. zones through θ' precipitation, allowing identification of each phase by its characteristic fringe spacing even when such evidence in the electron diffraction patterns was questionable. Similar applications to a Cu-Be alloy (Phillips and Tanner, 1973) permitted analysis of monolayer G.P. zones by {200} lattice images in spite of a very strong {110} tweed contrast. When utilized in an examination of the omega transformation in Zr-Nb, lattice imaging furthermore confirmed the existence of three subvariants within a previously identified single omega variant, (Chang et al., 1976) and led (Kuan and Sass, 1977) to the formulation of a new model for a linear, omega-like defect in these materials.

As shown by these studies, the most obvious advantage of high resolution electron microscopy is the enhanced structural detail which it can provide, enabling real space crystallography to be performed on even the most complex materials (Cowley and Iijima, 1972). Because the microscope is operated in a transmission mode, this type of information can furthermore be extracted from the vicinity of internal interfaces without the need for fracturing the specimen to expose the appropriate boundaries. Hence it is possible to study directly the atomic configurations at intact interfaces which are responsible for both the physical and mechanical behavior of materials. Such information is vitally important in the analysis of phase transformation behavior, i.e., the structure of the reaction front, and in the deformation behavior of polycrystals, i.e,, the structure at and near grain boundaries. Each of these points will be treated below, in particular for ordering and martensitic trans-

formations, and for grain boundary-related problems in both metallic and ceramic alloy systems.

1. Ordering Reactions

A fruitful area of application for high resolution electron imaging has been the study of short range order (Sinclair and Thomas, 1975) and ordering (Dutkiewicz and Thomas, 1975) in a number of alloy systems. For these investigations, experiments are designed to permit the imaging of the ordered superlattice planes as well as the fundamental lattice planes, when they coexist within the specimen. The most successful imaging technique has been to combine the transmitted, first order superlattice, and first order fundamental reflections along a systematic row within the objective aperture (Sinclair, et al., 1975). The illumination is also tilted to align the superlattice reflection on the optic axis. Because this situation results in a focus-dependent image (eq. 1), calculations must also be performed to ensure accurate image interpretation (Sinclair, et al., 1975; Dutkiewicz and Thomas, 1976). These points are illustrated below for the Mg-Cd systems (Sinclair and Dutkiewicz, 1977).

The ordering reaction in bulk Mg_3Cd results in the transformation of a disordered hcp lattice to the hexagonal DO_{19} structure. This sequence is altered however (Dutkiewicz and Sinclair, 1976) for very thin foils, wherein an orthorhombic B19 structure may evolve from either the hcp or DO_{19} phases. Utilizing the lattice imaging technique outlined above, highly detailed information has been obtained on the nature of both the order-disorder interface and domain boundary structure in this material.

At the proper imaging condition, the interface between ordered and disordered regions of the matrix should be distinguished by a transition from superlattice to fundamental fringe character. This condition was

<Fig. 2> obtained for partially ordered Mg_3Cd and as shown in Fig. 2, indicates that the interface is not a sharp one. Instead there appears to be a diffuse profile in degree of order over a distance of ~5 to 25Å, as indicated by the variation in fringe visibility at the interface.

In addition, lattice imaging has revealed the presence of interfacial dislocations at the boundary between larger ordered domains (Fig. 2) and the disordered matrix. Superlattice fringes (at bottom of Fig. 2) normally become bifurcated upon crossing the interface, and for the case of complete coherency, should merge continuously with the fundamental fringes (at top of Fig. 2). However the arrowed (001) superlattice fringe in Fig. 2 transforms to a single $(02\bar{2}0)$ fundamental fringe, indicating that an extra (002) atomic plane exists in the ordered phase and terminates at the interface. Hence the interfacial dislocation at this region is characterized by a fundamental lattice, not a superlattice, vector.

Other significant atomic level features have been observed in fully ordered Mg_3Cd, particularly at domain boundaries. The lattice image in

<Fig. 3> Fig. 3 shows a rotation domain boundary (RDB) in the fully ordered material which is seen to be atomically flat and approximately one atomic diameter in width. Notably there is also a step (arrowed) in the interface, which is exactly one unit cell dimension (5.3Å) in height. This observation suggests that domain growth may proceed by a ledge mechanism. The passage of these ledges along the interface can increase the size of one domain at the expense of its adjacent domain by the lateral motion of their shared boundary.

<Fig. 4> Further evidence for this effect is shown in Fig. 4, where the macroscopic curvature of the RDB is obviously produced by the arrowed facets. It is important to point out that such ledges were never observed to be

more than a single unit cell in height, obviously beyond the resolution limit of conventional dark field imaging techniques.

2. Martensitic Reactions

Martensitic reactions are of great significance technologically, e.g., in steels and shape-memory alloys. Whilst much has been written about the phenomenology of the transformation little is known in detail about martensite nucleation, growth, structure of the interfaces or what controls the nature of the inhomogeneous shear (slip or twinning). Clearly much can be learned by applying lattice imaging and here an example is shown of the potential of this technique for studies of complex dual-phase ferrite martensitic steels developed for improved strength: weight applications (Koo and Thomas, 1977(a)). These steels have excellent strength and formability and information is needed on the nature of the ferrite/martensite interface and also on the composition (i.e., solute distribution) of these phases. Lattice imaging is especially difficult because of the astigmatism corrections needed due to the ferromagnetism in steels (Koo and Thomas, 1977(b)).

<Fig. 5> Fig. 5 shows the ferrite (α)-martensite boundary in a transformed specimen of an Fe-2%Si-0.1%C alloy after quenching from the two phase ($\alpha + \gamma$) field at 850°C. The image was produced by combining the transmitted beam with the closely spaced 101 reflections of both the b.c.c. α phase and the b.c.t. martensite, under tilted illumination conditions. It is seen that the tetragonality of the martensite has induced a slightly larger interplanar spacing which is reflected in the measured variation of fringe spacing recorded on the micrograph. From this result the carbon content of the martensite phase was estimated to be ~0.3%. Thus the lattice imaging provides chemical information (Section III B) here which cannot be obtained by other methods.

The most significant feature of this image is the high degree of continuity of atomic structure across the α/martensite interface and the direct indication of structural discontinuities (arrowed) at the boundary. The former observation can be explained as a localized manifestation of the Kurdjumov-Sachs (K-S) orientation relationship at elevated temperatures. In this case the high temperature austenite (γ) (111) planes should parallel the (101) planes of the ferrite, such that during the transformation to martensite, $(111)_\gamma$ becomes $(101)_{martensite}$ parallel to $(101)_\alpha$.

Although they haven't yet been analyzed in detail, the arrowed fringe terminations in Fig. 5 indicate the presence of accommodation defects at the boundary. An exact assessment of such defects in this and the γ/martensite transformation interface is of particular interest in this field, and progress is currently being made in applications of high resolution imaging to this problem in shape-memory martensitic alloys, e.g., Ti-Ni (Sinclair, 1977).

3. Grain Boundaries in Alloys

Grain boundaries are known to catalyze a wide variety of solid state phase transformations which drastically affect metallurgical properties. The study of grain boundaries and the reactions which they influence has traditionally required transmission electron microscopy, but has recently (Gronsky, 1976) incorporated the high resolution techniques described above. One area of particular interest has been the relationship between grain boundary structure and grain boundary precipitation, where the finest details of boundary structure must be discerned and completely characterized.

An example is given by the plane matching (PM) model of grain boundary structure, which was originally proposed by Pumphrey(1972) in order to explain certain transmission electron microscopy observations of periodic

contrast features at grain boundaries. The basic premise of this model is that the matching of a set of close-packed planes across a grain boundary results in a low energy configuration. Since the matching is brought about by a periodic array of defects, it is responsible for a characteristic structure within the boundary.

Subsequent applications (Pumphrey, 1973) of the PM model to the description of grain boundary structures have met with success. Nevertheless each of these studies has had to rely heavily upon indirect evident (viz., electron diffraction information) due to the limited spatial resolution of the involved TEM techniques. Recently however an exact verification of plane matching conditions at a grain boundary has been obtained (Gronsky and Thomas, 1977(a)) utilizing high resolution electron microscopy. The proof is based upon a direct image of the mismatched atomic planes.

Periodic structural features observed within grain boundaries by TEM are given a simple optical representation in the PM theory. Idealizing the set of mismatched atomic planes on both sides of a boundary as a pair of optical gratings, the boundary region itself is depicted by their overlap (Fig. 6). Consequently the observed linear contrast features at the boundary may be visualized as a Moiré effect.

<Fig. 6>

In general the spacings d_1 and d_2 of the two misoriented lattices need not be the same, and as shown in Fig. 1, when rotated by an angle θ the overlapping gratings give rise to a Moiré fringe pattern (Hirsch, et al., 1965) of characteristic spacing:

$$d = \frac{d_1 d_2}{(d_1^2 + d_2^2 - 2d_1 d_2 \cos\theta)^{1/2}} \qquad \text{Eq. (2)}$$

Furthermore, the rotation angle (ρ) between the Moiré fringes and the fringes of grating 1 may be computed as:

$$\sin \rho = \frac{d_1 \sin \theta}{(d_1^2 + d_2^2 - 2d_1 d_2 \cos \theta)^{1/2}} \qquad \text{Eq. (3)}$$

In order to test the theory, an Al-9.5 at% Zn alloy was fabricated and aged to encourage grain boundary precipitation. Regions of precipitate/matrix interfaces at grain boundaries (satisfying $d_1 \neq d_2$) were surveyed and imaged in a tilted illumination mode. The objective aperture included only one strongly diffracted beam from each of the regions to be imaged as well as the transmitted beam.

<Fig. 7> The lattice image shown in Fig. 7(a) is an example of the type of micrograph used for analysis. Diffraction conditions are shown in Fig. 7(b). The figure includes simultaneous images of the (200)` planes from matrix [1], the $(1\bar{1}20)$ planes of the rhombohedrally distorted Zn-rich precipitate (P), and the (200) planes (at much lower visibility) from matrix [2].

Using the highly visible fringes in grain [1] as a magnification standard, their spacing (2.02Å) was measured from enlarged micrographs to within $\pm$ 0.01Å. By comparison the precipitate fringes were found to be spaced by 2.09 $\pm$ 0.01Å.

The rotation angle θ between matrix [1] and precipitate (P) fringes was determined from both lattice image and SAD (Fig. 7(b)) measurements to be 9.2 $\pm$ 0.1°. Applications of the Moiré formulae allowed the measured spacing (d) and rotation angle (ρ) of the boundary structural lines then to be compared with the calculated values (see also Fig. 1), as follows:

d meas. = 12.2 $\pm$ 0.5Å d calc. = 12.4 $\pm$ 0.2Å

ρ meas. = 106.5 $\pm$ 0.5° ρ calc. = 107 $\pm$ 1°

The results are in excellent agreement. At this level of resolution, tilting experiments failed to reveal the presence of any other structural lines within the boundary region.

The structural nature of the apparent Moiré fringes is revealed in <Fig. 8> Fig. 8 which is a high magnification image of the boundary region in Fig. 7(a). Here it is seen that continuity of mismatch is observed within the high density Moiré bands as evidenced by the presence of terminating fringes (arrowed). These terminations furthermore suggest that misorientation dislocations with a Burgers vector equal to the interplanar spacing may be associated with the misfit lines, in exact agreement with the PM theory.

4. Grain Boundaries in Ceramics

The properties of many ceramics, particularly the mechanical and electrical properties, are also largely influenced by their grain boundaries. These regions are of further interest since most ceramics are fabricated from powders by either sintering or hot pressing, both of which depend critically on the grain surfaces and boundaries. Despite their importance however little is known about them and even compared with our knowledge of grain boundaries in metals the study of ceramics at high resolution is very much in its infancy.

A common microstructural feature of many important ceramics, particularly those formed by a solution-reprecipitation process or by liquid phase sintering, is that they consist of a mixture of one or more crystalline phases and an additional "wetting" phase. When these ceramics are examined by optical microscopy the wetting phase appears to have a near-zero contact angle with the other phase(s) and this observation has led to the common assumption that the grains of the crystalline phase(s) are encompassed and separated by the "wetting" phase. Whether or not it does

indeed wet the grains to form a continuous grain boundary film is of great importance in relating macroscopic properties to the observed microstructure in order to improve the materials.

Two materials of contemporary interest stand out as examples in which a grain boundary film plays a crucial role in determining their properties; hot-pressed silicon nitride and the sintered ZnO based varistor material. In both a continuous intergranular film has been invoked to understand their behavior and high resolution electron imaging has subsequentially been used to detect and determine the distribution of the intergranular film. Electron imaging in the transmission electron microscope has proved to be the only technique capable of directly determining whether an intergranular film is present at a particular grain boundary, even though the film width may only be a few atomic layers thick.

a) Silicon Nitride

Dense silicon nitride is a strong polyphase ceramic and is a leading candidate for high termperature applications, such as in gas turbines (Burke, et al., 1974). It can be produced/fabricated by hot-pressing silicon nitride powders with a suitable sintering flux, such as magnesia, yttria, or ceria. However one of the barriers preventing its adoption at present is that its mechanical properties are severely degraded at temperatures exceeding 1300 ± 100°C; the exact temperature being dependent on compositional effects such as impurities and second phases. This <Fig. 9> is illustrated by Fig. 9 taken from the work of Lange (1974) in which the flexural strength of two commercial forms of silicon nitride, HS110 and HS130, are plotted against temperature. The HS110 is an early material containing relatively large proportions of glass forming constitutents

whereas the HS130 material is more recent and contains fewer impurities. Recent work (Lange, 1977) in the Si_3N_4-MgO-SiO_2 system has shown that the high temperature strength also depends on the MgO/SiO_2 ratio.

The strength degradation has generally been attributed to the presence of a glassy phase located between the silicon nitride grains, which at elevated temperatures rapidly decreases in viscosity with increasing temperature, flows and allows the grains to slide past one another (Kossowsky, et al., 1975; Lange, 1974; Lange, 1975). The glass is thought to be formed from the magnesia fluxing aid, the silica unavoidably present on the silicon nitride starting powders and the calcia impurities in the silicon nitride.

Because of its determining influence, several investigators have sought to detect and analyze the intergranular film by Auger electron spectroscopy, transmission electron microscopy and internal friction measurements.

Auger electron spectroscopy of inter-granular fracture surfaces combined with sputter etching indicates that Ca, O, Mg are concentrated within about 50-100Å of the grain boundaries (Kossowsky, 1973; Powell and Drew, 1974). By making up a material with a composition similar to that obtained from their Auger work, Powell and Drew concluded that the grain boundary film was probably a magnesium-calcium silicate having a softening temperature of approximately 1200°C. However in both sets of experiments, the information was obtained from an area of fracture surface of typically $3mm^2$--a total of approximately one million grains. High temperature internal friction measurements carried out by Mosher, et al., (1976) on commercial grades of silicon nitride demonstrate that viscous losses occur above ~800°C. Assuming that the glass is a magnesium-calcium silicate, the measured damping losses would be accounted for by a glassy layer

perhaps 50-100Å thick. However, as with the Auger electron spectroscopy results, the measurements are averaged over many grain boundaries, in this case over the entire volume of the material.

Although these experiments have yielded valuable evidence for the existence of the glassy phase at the grain boundaries, they are based upon techniques that are insensitive to the spatial distribution and location of the phase. In order to determine where the glassy phase is in the microstructure, a direct imaging technique with high spatial resolution is required.

Examination of three commercial silicon nitrides hot-pressed with MgO (HS110, HS130 and NC132) shows that the glassy phase is inhomogeneously distributed and in some regions large pockets of it can be seen commensurate in size to the silicon nitride grains. Thick layers separating grains can also be seen in some regions, as in Fig. 10. In general however the glassy phase is confined to the three grain junctions, as is dramatically revealed in the lattice fringe image of Fig. 11. Here the lattice fringes in the upper and lower right grain can be clearly seen, together with the extent of the phase A at the triple grain junction. The lattice fringe image also demonstrates that the phase decreases in thickness away from the junction but does not disappear altogether. Instead it forms a thin intergranular film ~8Å thick between the upper and lower right grains. (The grain at the lower left appears very dark since it is in a poorly transmitting orientation, but the Moiré fringes at B indicate that it is also crystalline.) Also in the figure, it can be seen that the overall shape of the phase, presumably the minimum energy configuration, is formed by interplanar high ledges in the interface. Unfortunately with the present state of the art it is not possible to ascertain whether

<Fig. 10>

<Fig. 11>

the phase is amorphous or crystalline because it is too small for interpretating diffraction information. However, the "granular" texture of the image suggests that it is amorphous (if there was simply a hole at the grain junction then the region would be featureless).

In addition to demonstrating that the glassy phase is predominately located at multiple grain junctions, lattice fringe imaging has also shown that a substantial proportion of the grain boundaries examined are devoid <Fig. 12> of any intergranular film. An example of this is Fig. 12. In this micrograph the lattice fringes are continuous right up to the boundary where they merge with the fringes from the adjacent grain, indicating that no intergraular film is present. The origin of the light band at the boundary is not clear but it is most probably a result of preferential grain boundary etching. In micrographs such as these the structure of the boundary itself can also be seen, for instance as the terminating fringes in the boundary. (These can be seen most easily by viewing the micrograph obliquely.)

Taken together, these and many other observations (Clarke, 1976; Clarke and Thomas, 1977) show that a continuous grain boundary phase does not exist at room temperature as has been envisaged. However these two contrasting views may be reconciled by recent theoretical work* which shows that a glass located only at triple grain junctions at low temperatures will penetrate between grains within seconds at high temperatures by a stress promoted solution-reprecipitation mechanism.

Following the identification of the detrimental role played by the magnesia additive in forming a glassy phase, it was found that superior high temperature strengths could be obtained by using yttria as a fluxing aid in place of the magnesia (Fazza, 1973). Subsequent investigations

by Rae, et al. (1975) explained the effectiveness of the yttria as being primarily due to the formation of an yttrium-silicon oxynitride, $Y_2Si(Si_2O_3N_4)$, which is stable in inert atmospheres to about 1600°C. However, although the use of yttria instead of MgO clearly leads to improved high temperature properties, the silicon nitride still suffers a degradation in strength. In order to determine whether there is a microstructural origin of this strength degradation, a silicon nitride hot pressed with 10 m/o Y_2O_3* has been examined by both electron microscopy (Clarke and Thomas, 1977) and by X-ray microanalysis using an electron microscope (Geiss and Clarke, 1977).

Two phases are apparent at relatively low magnifications, silicon nitride and the yttrium-silicon oxynitride. The relative amount of the oxynitride phase varies locally in the microstructure. In regions where it has a low volume fraction, it is located principally at the three and four grain junctions, whereas in those regions where it occupies a high volume fraction it surrounds the silicon nitride grains. In these cases, such as in Fig. 13, the silicon nitride grains are well facetted with a $\{1\bar{0}10\}$ habit. Observations such as these suggest strongly that the material densifies by a solution-reprecipitation mechanism.

<Fig. 13>

Closer examination of the material, however, reveals that an intergranular phase is present as a thin intergranular film (10-70Å) between the silicon nitride and yttrium-silicon oxynitride grains. No film is detectable at boundaries between silicon nitride grains. What the phase consists of is at the present time a matter of conjecture since it is too narrow to produce interpretable diffraction information. However, if it is an equilibrium phase, then according to a recently published phase behavior diagram (Lange, et al., 1977) it should be $YSiO_2N$, the nitrogen analog of pseudo-wollastorite.

The detection of such a thin film demonstrates the vital role that electron imaging can play in complementing other techniques of microstructural analysis. Without knowing that such a film was present, interpretations of depth profiling Auger electron spectroscopy or secondary ion mass spectroscopy analyses could lead to very misleading conclusions.

Lattice fringe images of the intergranular region also provide clues as to the mechanism of densification, as can be seen in Fig. 14. <Fig. 14> Here the junctions between a yttrium-silicon oxynitride grain, B, and two silicon nitride grains, A, in one of which the lattice fringes can be seen, are imaged. The intergranular phase, C, can clearly be seen to the left of the grain B and somewhat less evidently to the right. Apart from the presence of the intergranular film the striking feature of the silicon nitride grain boundary to the left is the presence of ledges, one interplanar spacing high. These micro-ledges, present at the interfaces between crystalline grains and intergranular phases, have proved to be common in all of the materials having an intergranular phase (Si_3N_4, MgSiAlON, BeSiN and ZnO), indicating that they are of widespread significance and possibly are the sites at which crystallization occurs.

One of the advantages of using the electron microscope to study the structure of materials is that elemental information can also be obtained with the same basic equipment. This is a rapidly expanding research area and involves detecting and analyzing the X-rays produced in the sample by the electron beam (Wells, 1974). Various schemes have been developed to perform X-ray microanalysis of regions a few hundred angstroms across and are now sold by the microscope manufacturers. One technique is particularly suited to obtaining both diffraction patterns from areas as small as 25Å across and X-ray microanalysis from areas of a few hundred

angstroms (Geiss, 1975(a); 1975(b)) using a conventional transmission microscope. This utilizes a condenser-objective lens configuration and has been successfully utilized in the microanalysis of 100Å diameter regions of a yttria hot-pressed silicon nitride (Geiss and Clarke, 1977(b)).

Using this equipment, preliminary X-ray microanalysis has revealed that the yttria hot-pressed silicon nitride is much more complex chemically than indicated by conventional X-ray powder diffraction. In particular the yttrium-silicon oxynitride phase is not pure, and can contain a variety of impurity elements. This is illustrated in Fig. 15 with a spectrum taken from a region of yttrium-silicon oxynitride grain approximately 3000Å in size. In addition to the yttrium and silicon which should be present, there are also substantial proportions of Fe, Mn, W, Cr and Cu (the copper peaks are fluorescence from the copper microscope grid on which the sample was mounted in the microscope). None of these elements are detected in the silicon nitride grains. The really interesting information as far as the ceramicist is concerned is that the actual impurity elements and their relative proportions change across the oxynitride grains, with dramatic changes occuring within distances as small as 150Å. These and similar findings reported elsewhere by Geiss and Clarke (1977(b)) support the suggestion of Rae, et al., (1975) that since the oxynitride phase is isostructural with the melilite silicates it should dissolve impurity elements, but these are the first observations as to the scale of distribution of the dissolved elements.

<Fig. 15>

Thus from these investigations using electron imaging two possible explanations for the degradation in strength of the yttria hot-pressed silicon nitride can be proposed. One is the presence of an intergranular film which at high temperatures may soften allowing grain sliding to occur,

as has been suggested for the magnesium hot-pressed material. The other is that the presence of large quantities of impurities in the yttrium-silicon oxynitride lowers the eutectic temperature, again allowing grain sliding to take place above a critical temperature.

b) Zinc Oxide Based Varistors

Metal oxide varistors are a class of semiconductor devices that exhibit very non-linear current-voltage characteristics, and which have found widespread use as electrical circuit protectors against transient voltage surges (Matsuoka, 1971; Harnder, et al., 1972). The commercially available varistors are fabricated by sintering zinc oxide powder with bismuth oxide and a number of other additives, the exact compositions being propriety information.

Normally pure zinc oxide behaves as an insulator and can be made conducting only by altering the stoichiometry, for instance, by adding excess zinc (Heiland, et al., 1959). However by adding small quantities of, for instance, bismuth oxide the material exhibits non-Ohmic electrical conduction. This extraordinary behavior has prompted several workers to investigate its origin in order to optimize it (Morris, 1973; Levinson and Philipp, 1975; Bernasconi, et al., 1976; Morris and Cahn, 1975). Most have postulated the presence of a highly resistive continuous intergranular layer separating the zinc oxide grains, and acting as an electrical barrier. Based on the presence of the layer, Levinson and Philipp (1975) have been able to explain the non-linear I-V characteristics in terms of Schottky current and Fowler-Nordheim tunneling.

However, experiments by Morris and Cahn (1975) investigating the Zno-Bi_2O_3 system, a prototype for the commercial material, indicate that a continuous grain boundary film does not form around the zinc oxide grains

and hence cannot account for the varistor behavior of the material. Firstly, by using as little as 0.008 m/o Bi_2O_3, which should be barely sufficient to coat the grains, varistor behavior was exhibited. Secondly, they observed that the Bi_2O_3 phase appeared at three and four grain junctions with a dihedral angle of approximately 60°--clearly too high an angle for it to wet the zinc-oxide grains and form a continuous grain boundary film. Thirdly, both Auger spectroscopic analysis and ion scattering spectroscopic analysis of fracture surfaces indicate that although the grain boundary is strongly enriched in Bi, it drops off rapidly over a distance of no greater than 20Å. This distance corresponds to the estimate of the upper limit to Gibbs absorption for pure Bi_2O_3 on zinc oxide, thereby indicating that an absorped layer, and not a film, is present on the grains.

The situation has been further clarified by high resolution electron imaging (Clarke, 1977) of a commercially available ZnO varistor incorporating Bi_2O_3, CoO, MnO, Cr_2O_3 and Sb_2O_3. These observations show that the Bi_2O_3 rich phase is localized at the three and four grain junctions and

<Fig. 16> in many cases can be seen to terminate abruptly, as in Fig. 16, and as found (Morris and Cahn, 1975) in the prototype material. In these cases the dihedral angle formed by the contact with the zinc oxide grains is non-zero, in the range of 12-85°. The variation is attributed to both the possible compositional variation in the Bi_2O_3 rich phase from one location to the next and any surface energy anisotropy of the zinc oxide. Furthermore in many of these boundaries, grain boundary dislocations may be observed, by their strain contrast, away from the three grain junction. Their presence is again indicative of there being no intergranular film, a conclusion that is supported by lattice fringe imaging of the boundary.

A relatively thick film is seen at some grain boundaries, as has been revealed in the lattice fringe image of Fig. 17, but this is unusual. Preliminary work suggests that the formation of the intergranular film has a crystallographic origin, since it only occurs at boundaries that are both straight and delineated by a basal plane in one of the adjacent grains (Clarke, 1977). This is clearly an area worthy of further investigation since it enables the microscopic aspects of wetting to be studied for the first time.

<Fig. 17>

B. Compositional Analysis

An additional advantage of high resolution electron imaging is the opportunity it provides for localized compositional analysis. In contrast to the spectroscopic (X-ray microanalysis) or microdiffraction techniques described above, this method relies exclusively on the imaging mode, and is, in principle, capable of spatial resolutions at the atomic plane level.

The technique is based on the application of Vegard's Law (assuming a linear relationship between lattice parameter and solute content). Measurements are made of fringe spacing variations which are produced by changes in interatomic spacing due to a composition variation in the specimen. When a measurement standard is present in the lattice image, e.g., a region of single phase or pure material with a well established lattice parameter, then it is possible to measure composition profiles on the same lattice image to within less than 1% error. Such measurements can be made from a scaling of direct photographic enlargements, from peak-to-peak distances on microdensitometer traces across the negative, or from optical diffractograms of the negative. The experimental accuracies of each of these methods are compared elsewhere (Sinclair and Thomas, 1977) and their application to the detection of localized composition profiles follows.

1. Spinodal Decomposition

Although the theory describing the spinodal transformation process is essentially complete (Cahn, 1968) there are serious deficiencies in the area of experimental characterization. Conventional methods, e.g., X-ray diffraction, resistivity measurements and transmission electron microscopy lack the spatial resolution necessary for a close examination of the decomposition process; therefore, the accuracy of existing theories cannot be tested. At present, a major area of interest is the measurement of localized composition amplitude (as well as wavelength) as a function of aging time. The only experimental method capable of providing acceptable levels of resolution for this study is lattice imaging electron microscopy (Gronsky, et al., 1975). By monitoring the interplanar separation reflected in the lattice image, small excursions in composition and corresponding atomic lattice modulations can be directly observed. This technique furthermore has the potential for revealing the full range of harmonics present in the modulated lattice. These harmonics are inevitably averaged out and therefore undetected by other techniques.

<Fig. 18> The micrograph shown in Fig. 18 was taken from a Au-77 at.% Ni specimen aged for 21 hours at 150°C. It displays both the fine lattice fringe periodicity of the (200) planes and the coarse variation in image contrast which is typical of a modulated microstructure imaged under two-beam conditions. Direct measurement of the coarse background contrast yields an average composition wavelength (λ) of 31 ± 5Å.

<Fig. 19> A plot of lattice fringe spacing against distance normal to a reference fringe is presented in Fig. 19. Each point n (n = 1,2,3...) on this plot represents the average of raw data points n to (n + 4) taken from a microdensitometer trace of the negative. The error bars indicate the

standard deviation introduced by the averaging process. The periodicity of the modulation from an extended analysis of this type, averaged over 12 wavelengths, is 29 ± 8Å, at an amplitude of $\lesssim$ 10%.

Satellites are clearly visible about the (400) spot in the electron
<Fig. 20> diffraction pattern (Fig. 20(a)) which records the tilted illumination imaging condition used to form this lattice image. The corresponding optical diffraction pattern (Fig. 20(b)) identically reproduces all essential diffraction effects, viz., the intense high angle and weak low angle satellites symmetrically positioned along <100> reciprocal lattice directions about <h00> fundamental lattice reflections. The difference in satellite intensities is due to the asymmetrical (Ni-rich) alloy composition. Complementary analysis of satellite spacings reveals that both diffraction patterns are also in excellent quantitative agreement. As determined from the electron diffraction patterns, $\lambda = 29 \pm 3$Å, while from the optical diffraction patterns, $\lambda = 29 \pm 2$Å.

Optical microdiffraction was also performed on this specimen using an aperture diameter less than the wavelength (Gronsky, et al., 1976).
<Fig. 21> Fig. 21 depicts the result for an aperture equivalent to ~20Å diameter at the specimen plane. By moving the aperture in ~10Å increments, an obvious variation in diffraction spot spacing is produced. In this case not only is the local wavelength rapidly recorded, but the local amplitude variation is captured as well. It is emphasized that the microdiffraction capabilities demonstrated by this example represent an improvement by three orders of magnitude (Sinclair, et al., 1976) over that attainable in conventional transmission electron microscopy.

Together these methods provide information on the composition variation essentially at an atom-plane to atom-plane level. Higher accuracies can

of course be anticipated for applications to materials having a large difference in component lattice parameters, as is the case with the Au-Ni system ($\Delta a \simeq 14\%$). However recent results have indicated a successful application (Wu, et al., 1977) of the technique to a commercial Cu-Ni-Cr alloy, where the difference in lattice parameters of the spinodal product is $\simeq 1\%$.

2. Grain Boundaries

The ability to detect highly localized compositional variations is a very desirable characteristic for experimental studies of grain boundaries. In current analyses of grain boundary precipitation reactions (Gronsky and Thomas, 1977(b)) by lattice imaging, fringe spacing measurements have given clear indications of composition profiles in the grain boundary vicinity with high precision. These results have been useful in identifying the involved reaction mechanisms and the particular role of grain boundaries in the precipitation processes.

<Fig. 22> Fig. 22 is an example of a lattice image of a grain boundary precipitate in an Al-9.5 at.% Zn alloy aged 30 mins. at 180°C. The boxed region in (a) is shown enlarged in (b), indicating the region on which compositional analysis was performed. Fringe spacings were measured within both matrix (top) and precipitate (bottom) areas, at increasing distances from the grain boundary. The results are presented in Fig. 23, each point indicating the average spacing of ten fringes, with a representative error bar shown on the first datum point.

<Fig. 23>

This plot clearly indicates a decreasing fringe spacing as the boundary (dotted line) is approached from either side. It suggests that a solute gradient exists within both the matrix and the precipitate, and that the concentration changes rapidly over a distance of only 50Å.

This technique also demonstrates high sensitivity for analysis of the earliest stages of growth, as shown in the next figure. The grain
<Fig. 24> boundary region running diagonally in Fig. 24(a) is imaged under the diffraction conditions shown in Fig. 24(b). An apparent thickening of the grain boundary region is observed, reaching a maximum width of ~55Å.

<Fig. 25> At higher magnification (Fig. 25) the fringes produced by the $(1\bar{1}\bar{1})$ planes of the upper grain are clearly visible. In addition there are lower visibility fringes within the thickened grain boundary region which are rotated clockwise at a small angle from the matrix fringes. Using the 2.33Å spacing of the $(1\bar{1}\bar{1})$ matrix planes as an internal magnification standard, it was found that the matrix lattice fringe spacing is constant to ±0.02Å measurement error. On this basis, the fringes within the boundary region have a spacing of 2.36 ± 0.02Å. The rotation angle is 2.8 ± 0.1°. Both spacing and angle agree qualitatively with the diffuse splitting seen in the electron diffraction pattern of Fig. 24(b); however no quantitative evaluation can be made from the pattern alone.

These results indicate that the larger spacing fringes actually represent a solute-enriched region independent of either bordering grain. The presence of very weak rotational Moiré fringes found only within this region (outlined by white slash marks in Fig. 25) further supports this description. The spacing and rotation angle of the Moiré pattern agree to within diffraction spot measurement error (~30% for this pattern) with the calculated values expected from the interference of the imaged second phase fringes and those lattice planes giving rise to the arrowed diffraction spike in Fig. 24(b) originating from the lower grain.

On the basis of its difference in interplanar spacings and rotation angle, the Zn-rich region was found to preserve its identity down to a thickness of ~6 to 8Å. The total length of grain boundary exhibiting second

second phase fringes was found to be 1500Å. This was also the approximate length over which the boundary coincided with the trace of the (200) planes of the upper grain, and suggests an orientation dependence which could not have been detected by alternative techniques.

IV FUTURE DIRECTIONS

The work presented here represents only an initial step towards the complete atomic characterization of materials. The most desirable progression of such research should lead to the attainment of structural images similar to those that are currently being used to explore the atomic arrangements in mineralogical specimens (Iijima and Allpress, 1974). As pointed out in section II, this requires only a slight improvement in the contrast transfer characteristics of present day electron optics.

The resolution limit (Δx) determining the finest level of specimen detail which can be directly interpreted in terms of the atomic structure of a specimen is roughly given by (Cowley, 1975),

$$\Delta x \simeq 0.6\ C_s^{1/4} \lambda^{3/4} \qquad \text{Eq. (4)}$$

indicating that although some advantage will be realized by improved lens design (decreased C_s), much greater benefit will emerge from the attainment of stable, high accelerating voltages (decreased λ) in transmission electron microscopy.

With this incentive, high voltage, high resolution electron microscopes are currently being constructed in Europe and Japan, and a 500 kV machine at the University of Kyoto has already successfully demonstrated its capabilities in atomic resolution (Krivanek, et al., 1977). Unfortunately the cost of such instrumentation has no precedent in this country for materials

science research funding, and will require a consolidated effort for its acquisition and continued development (Thomas, et al., 1976). As this instrumentation becomes available however, interpretable images of individual atoms and their environments can be routinely utilized in the solution of materials problems.

V SUMMARY AND CONCLUSIONS

The applications of high resolution imaging presented in this article illustrate a new dimension in electron microscopy which has only recently come of age. With proper care, modern TEM's can be made to produce images of this quality using specimens that are prepared by conventional techniques; however the interpretation of fine detail in high resolution images rquires an accurate knowledge of specimen thickness and orientation, as well as the major microscope parameters (C_s, λ), and operating conditions.

To date the advantages of high resolution electron imaging have been revealed in a wide variety of metallic systems, providing insight into the mechanisms of such phase transformations as ordering, spinodal decomposition, grain boundary precipitation, and the martensitic reaction. Structural discontinuities in interphase interfaces (atomic plane ledges) and grain boundaries (plane matching defects) have been identified with high precision, and compositional variations on an atomic scale have been detected, including solute segregation within ~10Å of a grain boundary.

In the study of ceramics, primary effort has been directed toward the detection of thin intergranular films with notable success. Atomic dimention microledges have also been revealed in crystallization interfaces, polytype boundaries and transformation fronts, and compositional variations near grain boundaries have recently been recorded in lattice images of a

Magnesium Sialon. It therefore appears that the technique holds equal promise for analyses of the fundamental mechanisms of crystallization, phase transformations, diffusion and solute segregation in ceramics as well as metallic alloy systems.

In the near future, high voltage, high resolution electron microscopy will make possible interpretable atomic resolution in these and most other commercial materials, allowing direct visualization of the arrangement of atoms in solids. Once this capability has been achieved, it will be extremely useful to be able to identify the atoms comprising the imaged structure, uniquely and individually. Such a development must then be made the next goal in the dual microscopic-spectroscopic characterization of materials.

ACKNOWLEDGEMENTS

The work on ordering was performed in our laboratory by Dr. R. Sinclair (now at Stanford University) and Dr. J. Dutkiewicz (of the Polish Academy of Sciences). Financial support from the United States Department of Energy, Division of Basic Energy Sciences, through the Materials and Molecular Research Division of Lawrence Berkeley Laboratory (R.G., G.T.) and from the National Science Foundation (D.R.C) is gratefully acknowledged.

FOOTNOTES

1. Page 18. F. F. Lange, private communication.

2. Page 19. Kindly supplied by F. F. Lange, Science Center, Rockwell International.

REFERENCES

1. Allpress, J. G. and Sanders, J. V. (1973). J. Appl. Cryst. 6, 165-190.

2. Bernasconi, J., Klein, J. P., Knecht, B. and Strassler, S. (1976). J. Elect. Materials 5, 473-495.

3. Born M., and Wolf, E. (1975). "Principles of Optics." 5th Ed., Pergamon Press, Inc., New York.

4. Burke, J. J., Gorum, A. E., and Katz, R. N. (eds.) (1974). "Ceramics for High Performance Applications." Brook-Hill, New York.

5. Bursill, L. A., and Wilson, A. R. (1977). Acta Cryst. A33, 672-676.

6. Cahn, J. W. (1968). Trans. Met. Soc. AIME 242, 166-180.

7. Chang, A. L. J., Sass, S. L., and Krakow, W. (1976). Acta Met. 24, 29-36.

8. Clarke, D. R. (1976). In "Nitrogen Ceramics" (F. Riley, ed.), Noordhoff International Publishers, Massachusetts.

9. Clarke, D. R. (1977(a)), J. Appl. Phys. (Submitted).

10. Clarke, D. R. (1977(b)). J. Am. Ceram. Soc. 60, 539-540.

11. Clarke, D. R., Shaw, T. M., and Thompson, D. P. (1977). J. Materials Science (In Press).

12. Clarke, D. R., and Thomas G. (1977(a)). J. Am. Ceram. Soc. 60, 491-495.

13. Clarke, D. R., and Thomas G. (1977(b)). J. Am. Ceram. Soc. (In Press).

14. Clarke, D. R., and Thomas G. (1977(c)). In "Processing of Crystalline Ceramics " (R.F. Davies, ed.) (In Press).

15. Cockayne, D. J. H., Parsons, J. R., and Hoelke, C. W. (1971). Phil. Mag. 24, 139-153.

16. Cowley, J. M. (1975). "Diffraction Physics." North-Holland Publishing Co., Amsterdam.

17. Cowley, J. M., and Iijima, S. (1972). Z. Naturforsch. 27a, 445-451.

18. Dowell, W. C. T. (1963). Optik 20, 535-568.

19. Dutkiewicz, J., and Sinclair, R. (1976). Scripta Met 10, 489-493.

20. Dutkiewicz, J., and Thomas, G. (1975). Met. Trans. 6A, 1919-1928.

21. Dutkiewicz, J., and Thomas, G. (1976). Thin Solid Films 32, 329-332.

22. Gazza, G. (1973). J. Am. Ceram. Soc. 56, 662.

23. Geiss, R. H. (1975(a)). Appl. Phys. Lett. 27, 174-176.

24. Geiss, R. H. (1975(b)). 33rd Ann. Proc. Electron Microscopy Soc. Amer. Las Vegas, 1975. (G. W. Bailey, ed.), 33-34.

25. Geiss, R. H., and Clarke, D. R. (1977(a)). 35th Ann. Proc. Electron Microscopy Soc. Amer. Boston, 1977. (G.W. Bailey, ed.), 35-37.

26. Geiss, R. H., and Clarke, D. R. (1977(b)). J. Ultrastr. Res. (Submitted).

27. Gronsky, R. (1976). Ph.D. Thesis, University of California, Lawrence Berkeley Laboratory, LBL-5784.

28. Gronsky, R., and Thomas, G. (1977(a)). Scripta Met. 11, 791-794.

29. Gronsky, R., and Thomas, G. (1977(b)). 35th Ann. Proc. Electron Microscopy Soc. Amer. Boston 1977. (G. W. Bailey, ed.), 116-117.

30. Gronsky, R., Okada, M., Sinclair, R., and Thomas, G. (1975). 33rd Ann. Proc. Electron Microscopy Soc. Amer. Las Vegas, 1975. (G. W. Bailey, ed.), 22-24.

31. Gronsky, R., Sinclair, R., and Thomas, G. (1976). 34th Ann. Proc. Electron Microscopy Soc. Amer. Miami Beach, 1976. (G. W. Bailey, ed.), 494-495.

32. Harnder, J. D., Martzoff, F. D., Morris, W. G., and Golder, F. D. (1972). Electronics 45, 91-95.

33. Heidenreich, R. D. (1964). "Fundamentals of Transmission Electron Microscopy." Interscience, New York.

34. Heiland, G., Mollwo, E., and Stoeckmann, F. (1959). Solid State Physics. (F. Seitz and D. Turnbull, eds.) 8, 193-326.

35. Hirsch, P. B., Howie, A., Nicholson, R. B., Pashley, D. W., and Whelan, M. J. (1965). "Electron Microscopy of Thin Crystals," Butterworths, London.

36. Howe, L. M., and Rainville, M. (1972). Rad. Eff. 16, 203-209.

37. Iijima, S., and Allpress, J. G. (1974). Acta Cryst. A30, 22-29.

38. Komoda, T. (1966). Jap. J. Appl. Phys. 5, 603-607.

39. Koo, J. Y., and Thomas, G. (1977(a)). Met. Trans. 8A, 525-528.

40. Koo, J. Y., and Thomas, G. (1977(b)). 35th Ann. Proc. Electron Microscopy Soc. Amer. Boston, 1977. (G. W. Bailey, ed.), 118-119.

41. Kossowsky, R. (1973). J. Mat. Sci. 8, 1603-1615.

42. Kossowsky, R., Miller, D. G., and Diaz, E. S. (1975). J. Mat. Sci. 10, 983-997.

43. Krivanek, O. L., Isoda, S., and Kobayashi, K. (1977). Phil. Mag. 36, 931-940.

44. Kuan, T. S., and Sass, S. L. (1977). Report #2803, Materials Science Center, Cornell University, Ithaca, New York.

45. Lange, F. F. (1974). J. Am. Ceram. Soc. 57, 84-87.

46. Lange, F. F. (1975). In "Deformation of Ceramic Materials" (R. C. Bradt and R. E. Tressler, eds.), pp 361-381, Plenum Press, New York.

47. Lange, F. F. (1977). J. Am. Ceram. Soc. (In Press).

48. Lange, F. F., Singhal, S. C., and Kuznicki, R. C. (1977). J. Am. Ceram. Soc. 60, 249-252.

49. Levinson, L. M., and Philipp, J. R. (1975). J. Appl Phys. 46, 1332-1341.

50. Misell, D. L. (1973). J. Phys. A. 6, 62-78.

51. Morris, W. G., (1973). J. Am. Ceram. Soc. 56, 360-364.

52. Morris, W. G., and Cahn, J. W. (1975). In "Grain Boundaries in Engineering Materials" (J. W. Walter, ed.), pp. 223-233. Claitor's, New York.

53. Mosher, D. R., Raj, R., and Kossowsky, R. (1976). J. Mat. Sci. 11, 49-53.

54. Matsuoka, M. (1971). Japan. J. Appl. Phys. 10, 736-746.

55. Parsons, J. R., and Hoelke, C. W. (1969). J. Appl. Phys. 40, 866-872.

56. Parsons, J. R., and Hoelke, C. W. (1970). Phil. Mag. 22, 1071-1074.

57. Parsons, J. R., Rainville, M., and Hoelke, C. W. (1970). Phil. Mag. 21, 1105-1117.

58. Phillips, V. A. (1972). Acta Met. 20, 1143-1156.

59. Phillips, V. A. (1973). Acta Met. 21, 219-228.

60. Phillips, V. A. (1975). Acta Met. 23, 751-767.

61. Phillips, V. A., and Hugo, J. A. (1970). Acta Met. 18, 123-135.

62. Phillips, V. A., and Tanner, L. E. (1973). Acta Met. 21, 441-449.

63. Phillips, V. A., and Wagner, R. (1973). J. Appl. Phys. 44, 4252-4254.

64. Powell, B. D., and Drew, P. (1974). J. Mat. Sci. 9, 1867-1870.

65. Pumphrey, P. H. (1972). Scripta Met. 6, 107-110.

66. Pumphrey, P. H. (1973). Scripta Met. 7, 1043-1046.

67. Rae, A.W.J.M., Thompson, D. P., Pipkin, N. J., and Jack, K. H. (1975). In "Special Ceramics 6" (P. Popper, ed.), pp. 347-360, Brit. Ceram. Res. Assoc.

68. Scherzer, O. (1948). J. Appl. Phys. 20, 20-29.

69. Sieber, P., and Tonar, K. (1975). Optik 42, 375-380.

70. Sinclair, R. (1977). 35th Ann. Proc. Electron Microscopy Soc. Amer. Boston, 1977. (G. W. Bailey, ed.), 110-113.

71. Sinclair, R., and Dutkiewicz, J. (1977). Acta Met. 25, 235-249.

72. Sinclair, R., and Thomas, G. (1975). J. Appl. Cryst. 8, 206-210.

73. Sinclair, R., Gronsky, R., and Thomas, G. (1976). Acta Met. 24, 789-796.

74. Sinclair, R., and Thomas, G. (1977). Acta Met. 25, 231-234.

75 Sinclair, R., Schneider, K., and Thomas, G. (1975). Acta Met. 23, 873-883.

76. Shaw, T. M., and Clarke, D. R. (1977). In "Processing of Crystalline Ceramics" (R. F. Davis, ed.) (In Press).

77. Skarnulis, A. J., Iijima, S., and Cowley, J. M. (1976). Acta Cryst. A32, 799-805.

78. Thomas, G. (1962). "Transmission Electron Microscopy of Metals." J. Wiley and Sons, Inc., New York.

79. Thomas, G., Glaeser, R., Cowley, J. M., and Sinclair, R. (1976). Proc. of Workshop on High Resolution Electron Microscopy, Lawrence Berkeley Laboratory Pub. 106.

80. Thomas, G., Van Der Biest, O. O., and Clarke, D. R. (1977). In "Ceramic Microstructures '76" (R. M. Fulrath and J. A. Pask, eds.), pp. 29-53, Westview Press, Boulder, Colorado.

81. Wells, O. C. (1974). "Scanning Electron Microscopy." McGraw-Hill, New York.

82. Wu, C. K., Sinclair, R., and Thomas, G. (1977). Met. Trans. (In Press).

FIGURE CAPTIONS

Fig. 1 Ray diagram for the two-beam tilted-illumination method of lattice imaging.

Fig. 2 Lattice image of partially ordered Mg_3Cd showing the order-disorder interface. The gradual transition from fundamental lattice fringe type indicates a degree of order profile at the interface. A misfit dislocation at the interface is also indicated, stemming from the presence of an extra fundamental lattice plane within the order domain.

Fig. 3 Lattice image of a rotation domain boundary in fully ordered B19 Mg_3Cd, showing the interface to be highly planar apart from the presence of a single unit-cell-high (5.3Å) ledge (arrowed).

Fig. 4 Lattice image of a rotation domain boundary showing the presence of several steps (arrowed) of unit cell (5.3Å) height in the curved interface.

Fig. 5 Ferrite-martensite boundary in a transformed Fe-2%Si-0.1%C alloy. The lattice image was produced by combining the transmitted beam with the closely spaced 101 reflections of both phases, and the tetragonality of the martensite is directly recorded in the fringe spacing variation.

Fig. 6 Optical analogue for the plane matching model. The Moiré pattern of spacing d is produced by overlapping gratings d_1 and d_2 misorientated by θ. The angle between the Moiré bands and the fringes of grating 1 is ρ.

Fig. 7 (a) Lattice image of the (200) planes from grains [1] and [2] as well as the $(11\bar{2}0)$ planes from the grain boundary precipitate [P] which they border. The fringes seen in the lower grain are spaced 2.02Å apart in this Al-9.5 at.% Zn alloy.
(b) Diffraction conditions used (a).

Fig. 8 Enlargement of the interphase boundary in Fig. 7 (fringes in lower grain have a spacing of 2.02Å). Open arrows indicate terminating fringes in optically dense regions.

Fig. 9 Flexural strength vs. temperature for HS-110 and HS-130 hot-pressed Si_3N_4 (specimen configuration, weak direction; crosshead speed, 0.02 in./min.).

Fig. 10 T.E.M. image of commercial silicon nitride hot-pressed with MgO. Thick intergranular layer is indicated at "P".

Fig. 11 Lattice image of a three-grain junction in silicon nitride showing the location of the amorphous phase "A". The fringe spacing in both grains is 6.6Å, and the amorphous phase is seen to extend between the grains to a thickness of ~8Å.

Fig. 12 Lattice image of a grain boundary in silicon nitride showing the absence of any intergranular film. The $(10\bar{1}0)$ interplanar spacing imaged in this micrograph is 6.6Å.

Fig. 13 Microstructure of yttria-fluxed material showing facetted silicon nitride grains with a {1010} habit amidst the yttrium-silicon oxynitride phase.

Fig. 14 Lattice image of the junction between a yttrium-silicon oxynitride grain, B, and two silicon nitride grains, A. The arrowed micro-

Fig. 14 ledges are possible sites for initiation of crystallization.

Fig. 15 X-ray spectrum from a region of a yttrium-silicon oxynitride grain approximately 3000Å in size.

Fig. 16 Triple grain junction in a commercial ZnO varistor. The dark region at the junction is the Bi_2O_3 rich phase which does not extend along the boundary, as evidenced by the presence of grain boundary dislocations (arrowed).

Fig. 17 Lattice image of the same varistor material as in Fig. 16 above showing an unusually thick intergranular film, P.

Fig. 18 Lattice image of a spinodally decomposed Au-77 at.% Ni alloy aged 21 hrs. at 150°C. Note both the fine scale periodicity of the (200) lattice planes and the coarse periodicity of the composition modulation.

Fig. 19 Plot of fringe spacing as measured from a microdensitometer trace normal to the fringes in Fig. 18. Each point n (n = 1,2,3...) represents the average of measurements n to (n + 4). The average wavelength indicated by this process is 29±8Å.

Fig. 20 Comparison of (a) the electron diffraction pattern corresponding to Fig. 18, and (b), the optical diffraction pattern taken from the lattice image negative. Satellites (s) about the fundamental reflections (f) agree in both spacing and relative intensities for the two patterns.

Fig. 21 Results of an optical microdiffraction analysis of Fig. 18 wherein an aperture equivalent to ~20Å at the specimen plane was translated across the negative normal to the fringes in

Fig. 21 in ~10Å increments. A periodic variation in spot spacing rather than satellites (central image) is produced because the aperture diameter is less than one composition wavelength (~29Å).

Fig. 22 Lattice image of a grain boundary precipitate in an Al-9.5 at.% Zn alloy shown at low magnification (a) and in an enlargement of the boxed region(b). The spacings of the fringes within the upper grain and the precipitate are shown in Fig. 23.

Fig. 23 Plot of fringe spacing vs. distance taken from Fig. 22(b) at increasing distances from the grain boundary (dotted line). Each point represents the average of ten measurements (an error bar is indicated on the first point) and clearly shows a gradient which can be related to the composition variation.

Fig. 24 Low magnification micrograph of a grain boundary region (a) in an Al-9.5 at.% Zn alloy with the corresponding diffraction conditions (b) for lattice imaging. An apparent thickening of the boundary (up to ~55Å) is observed.

Fig. 25 Higher magnification image of Fig. 24(a), showing the $(1\bar{1}\bar{1})$ planes of the upper grain at 2.33±0.02Å spacing, as well as the fringes within the boundary region at 2.36±0.02Å spacing. The Moiré pattern (outlined in white) further attests to the Zn enrichment at the boundary.

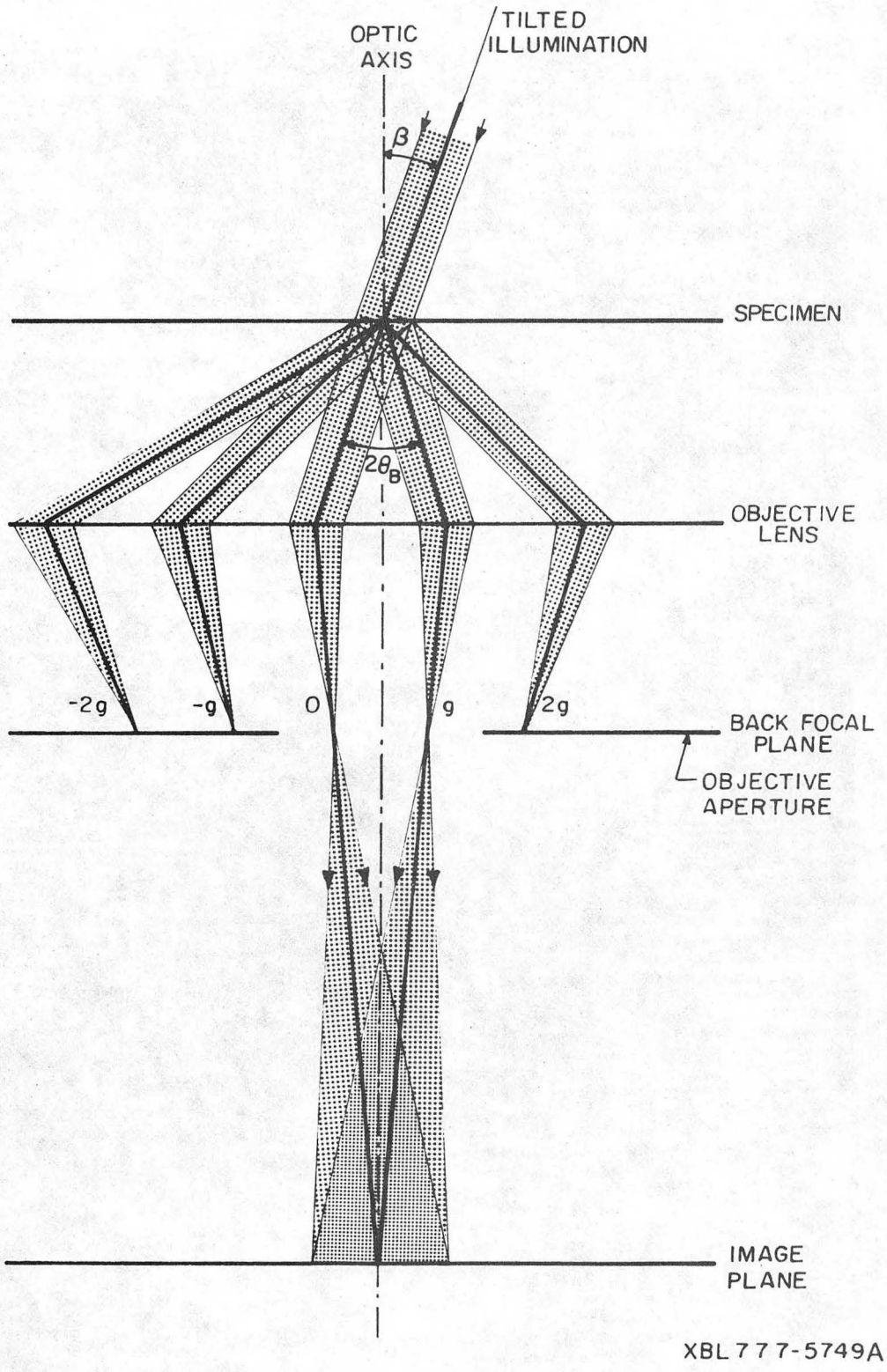
OPTIC AXIS
TILTED ILLUMINATION
β
SPECIMEN
2θB
OBJECTIVE LENS
-2g
-g
0
g
2g
BACK FOCAL PLANE
OBJECTIVE APERTURE
IMAGE PLANE
XBL777-5749A

Fig. 1

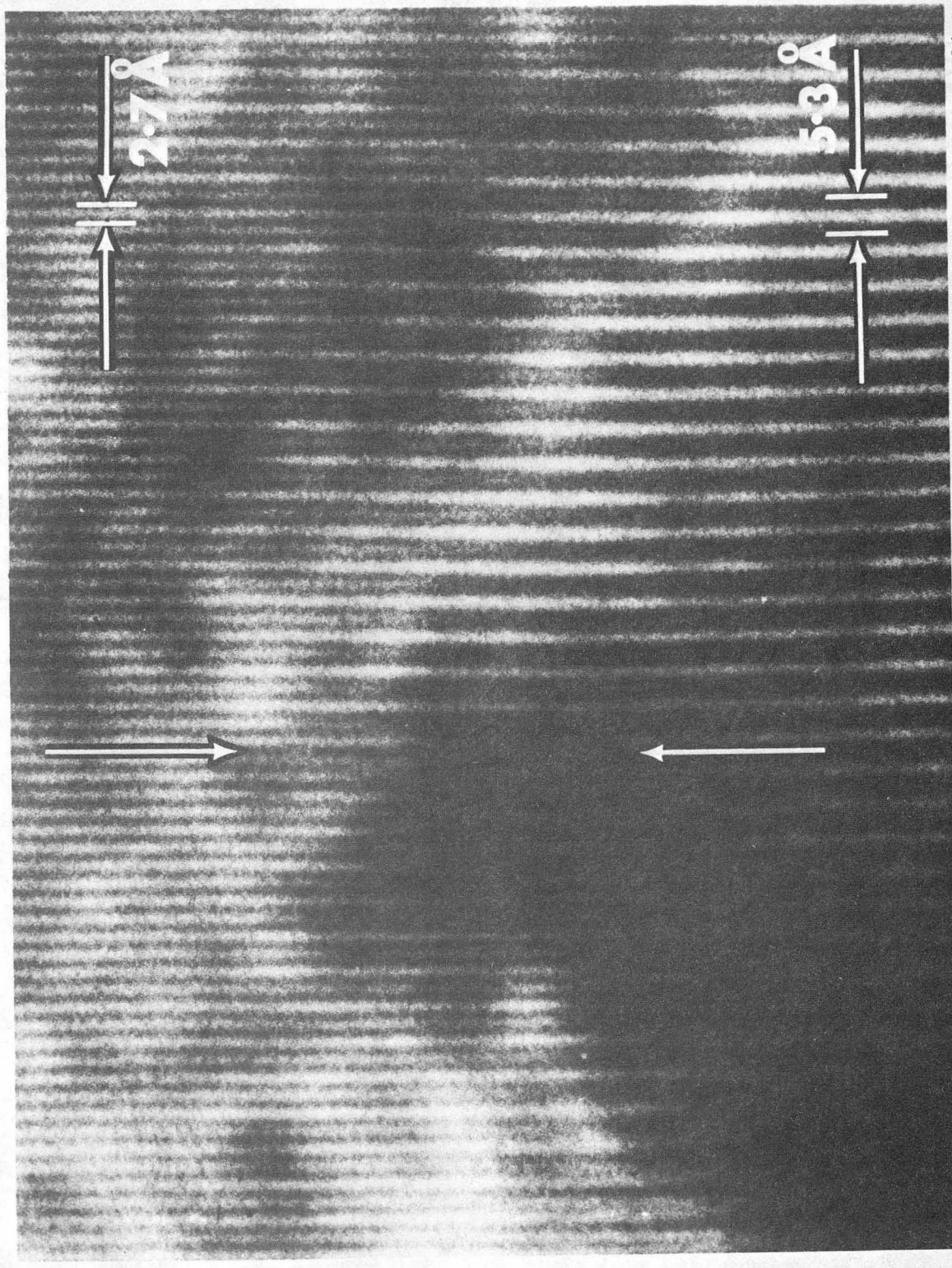

XBB 766-5784

Fig. 2

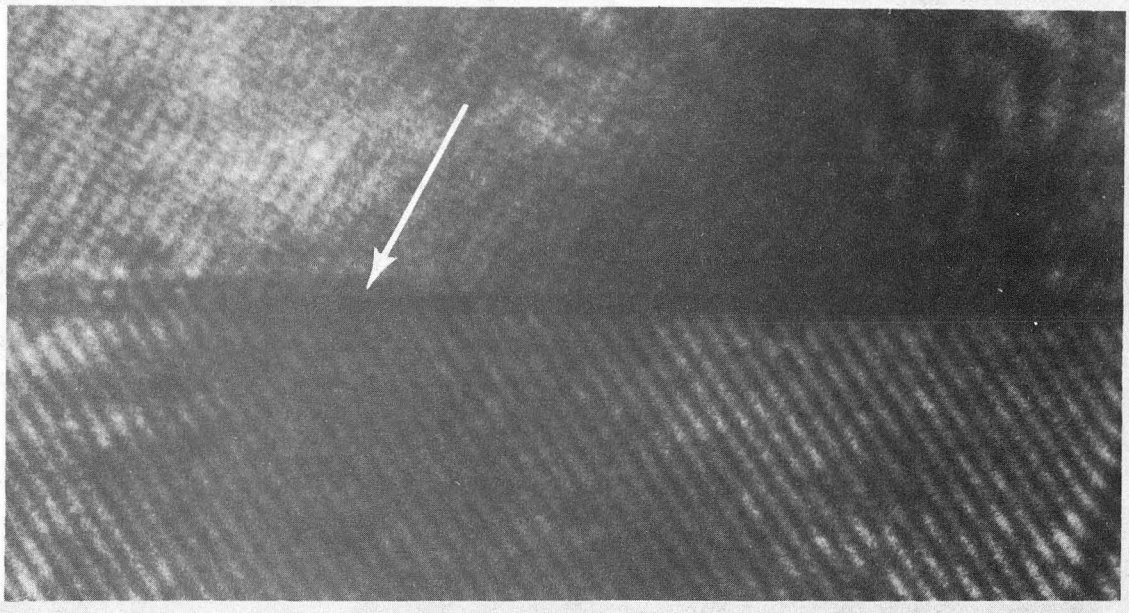

Fig. 3

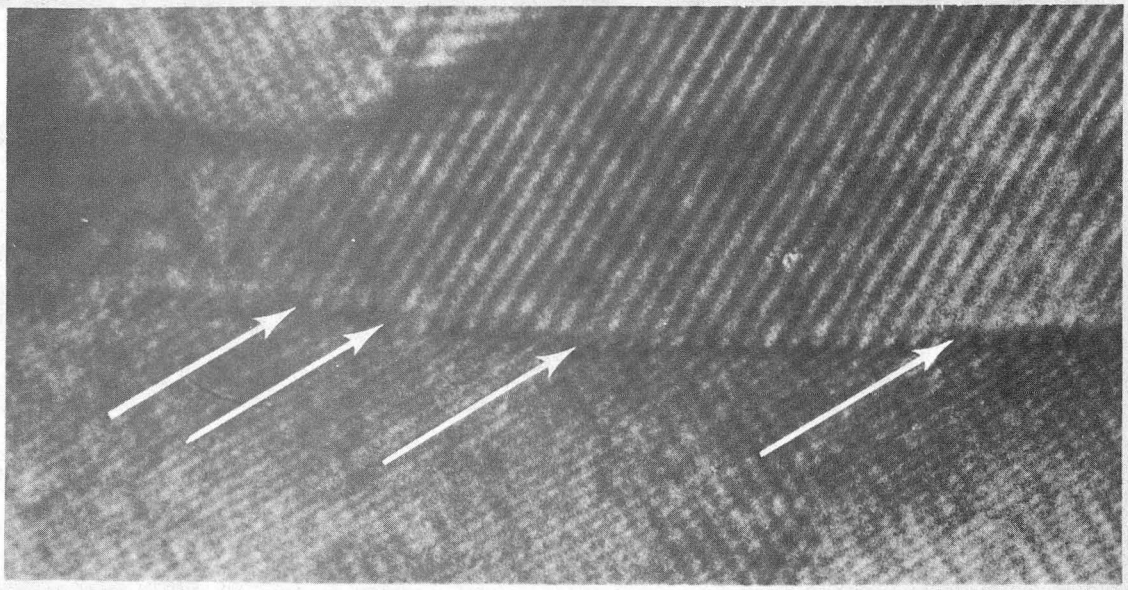

XBB766-5696

Fig. 4

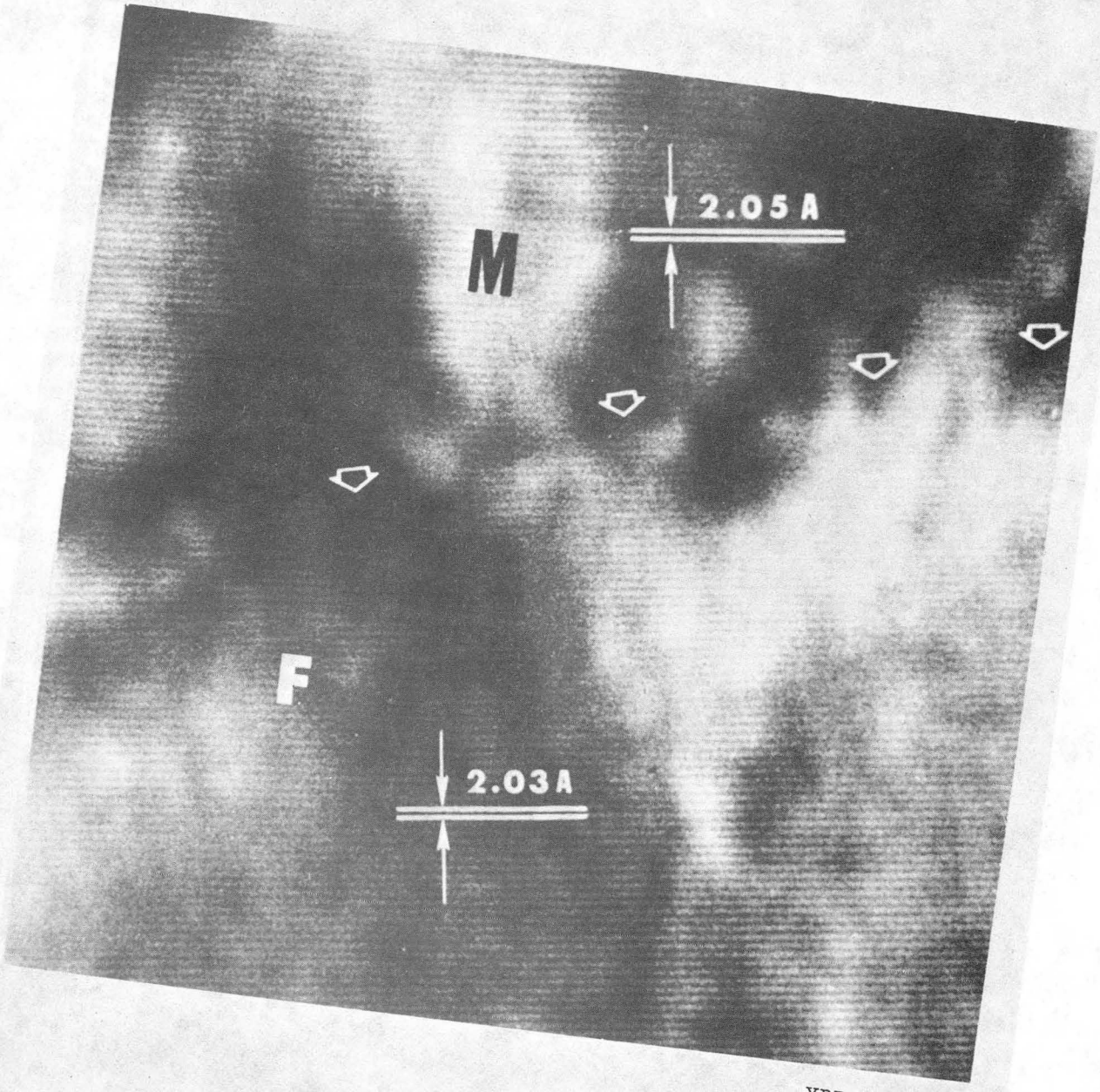

XBB 773-2297

Fig. 5

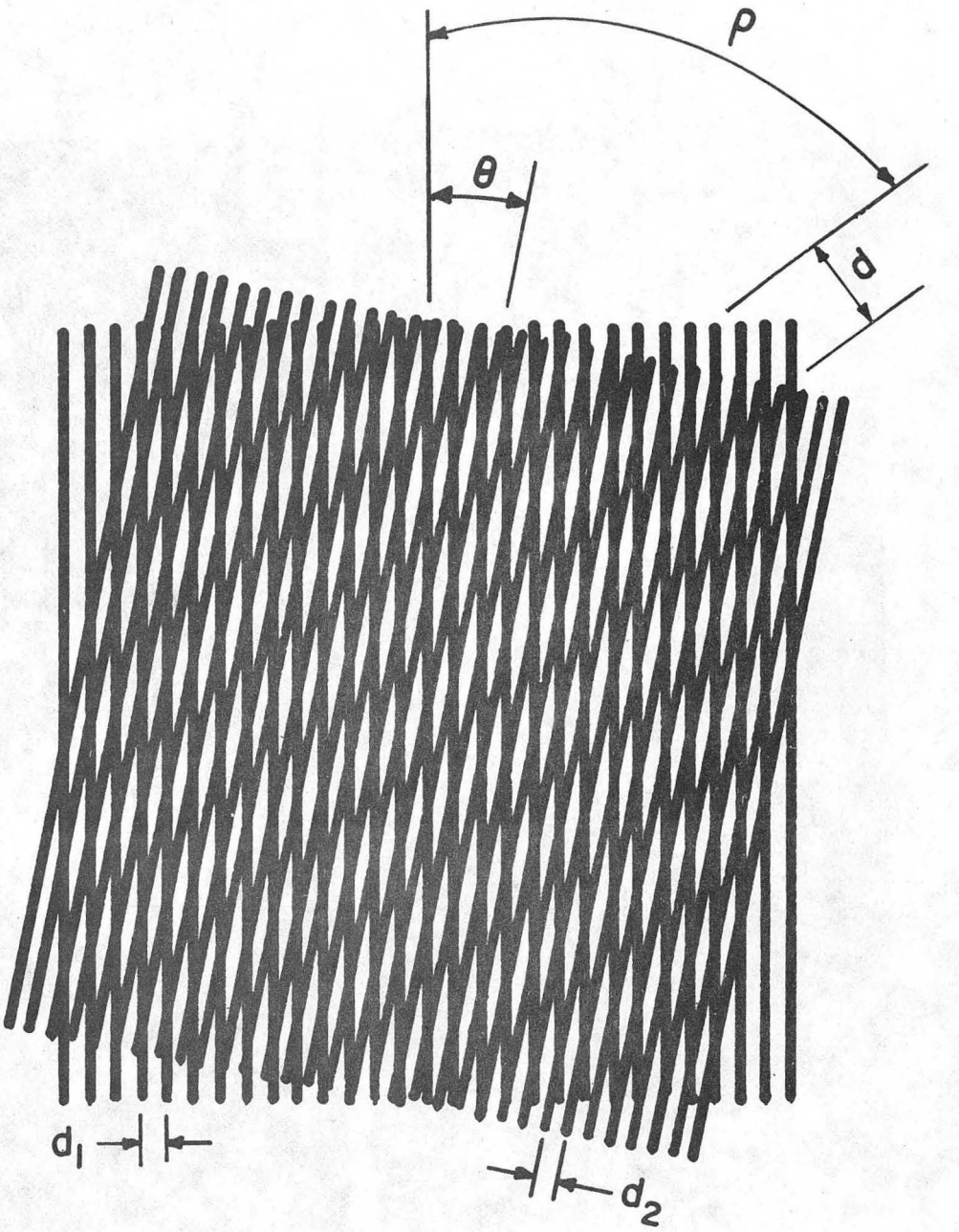

Fig. 6

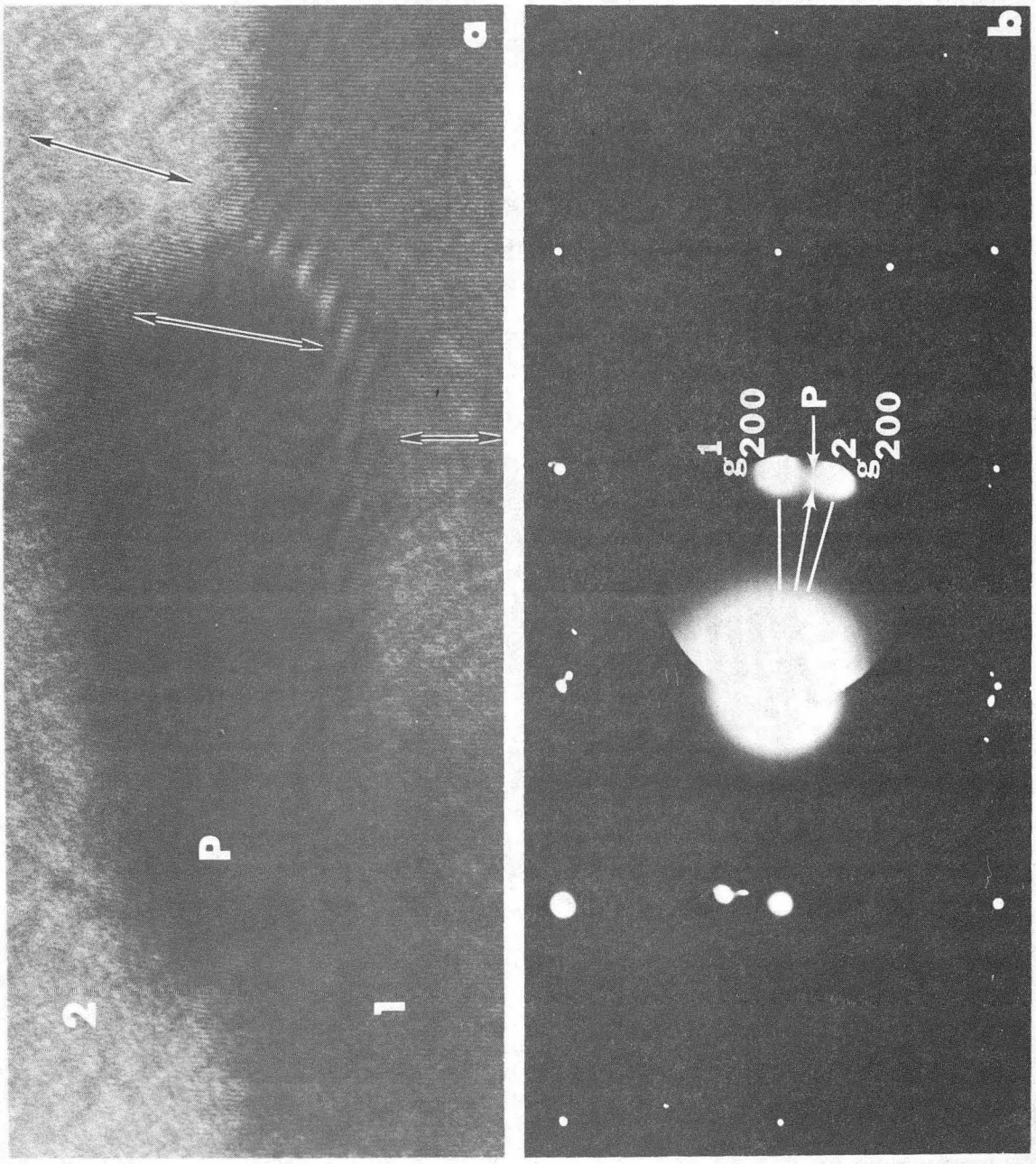

XBB 767-6532

Fig. 7

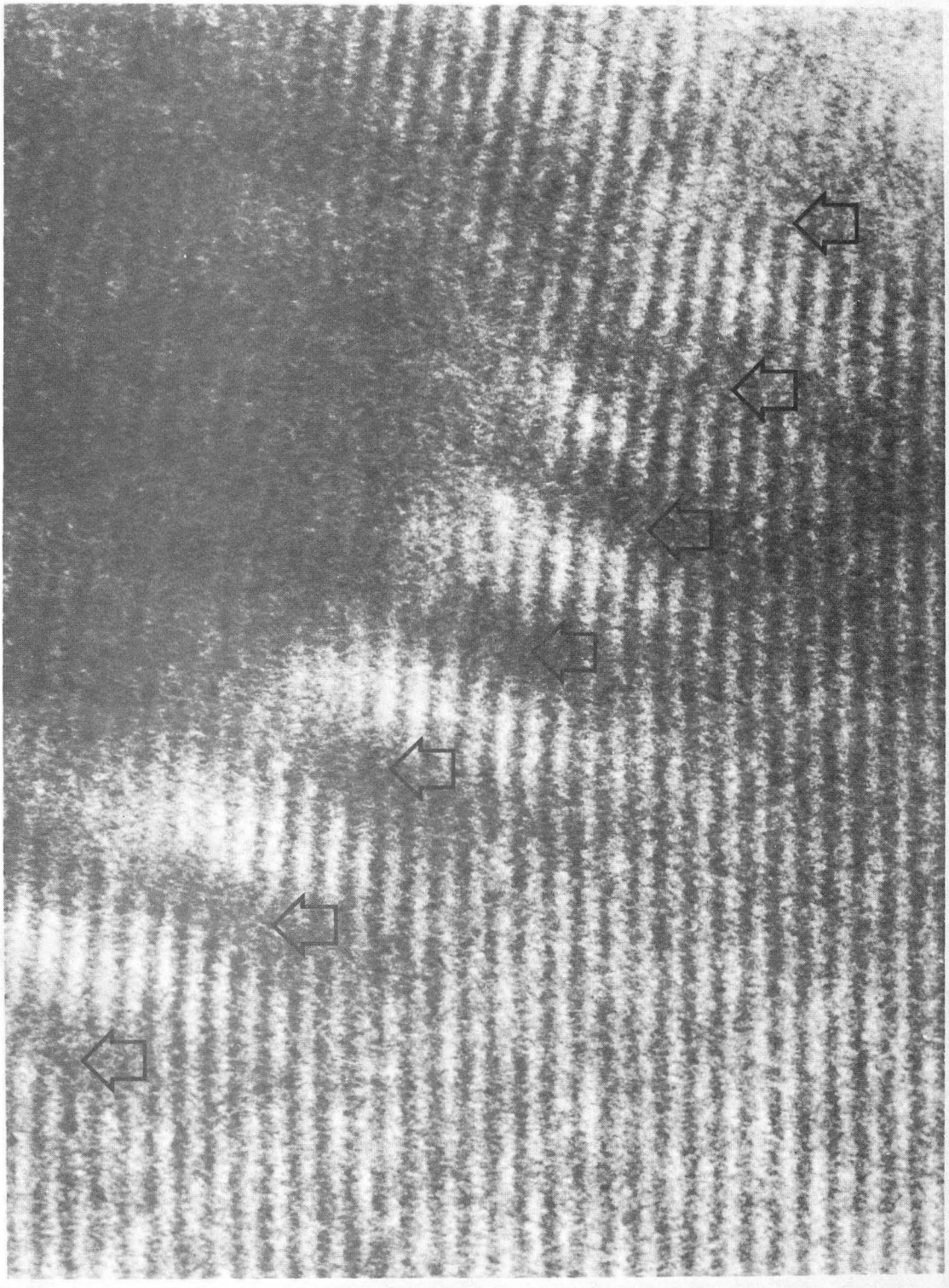

XBB 767-6627

Fig. 8

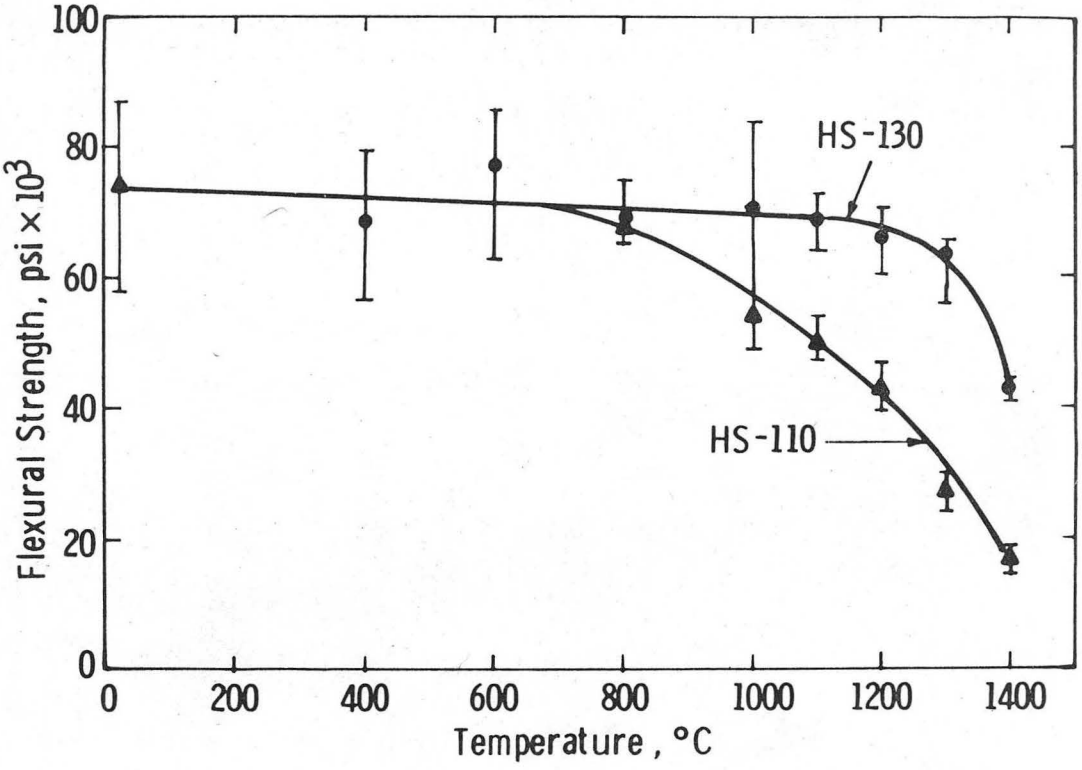

Flexural strength vs temperature for HS–110 and HS–130 hot-pressed Si_3N_4 (specimen configuration, weak direction; crosshead speed, 0.02 in./min).

XBL 7611-9787

Fig. 9

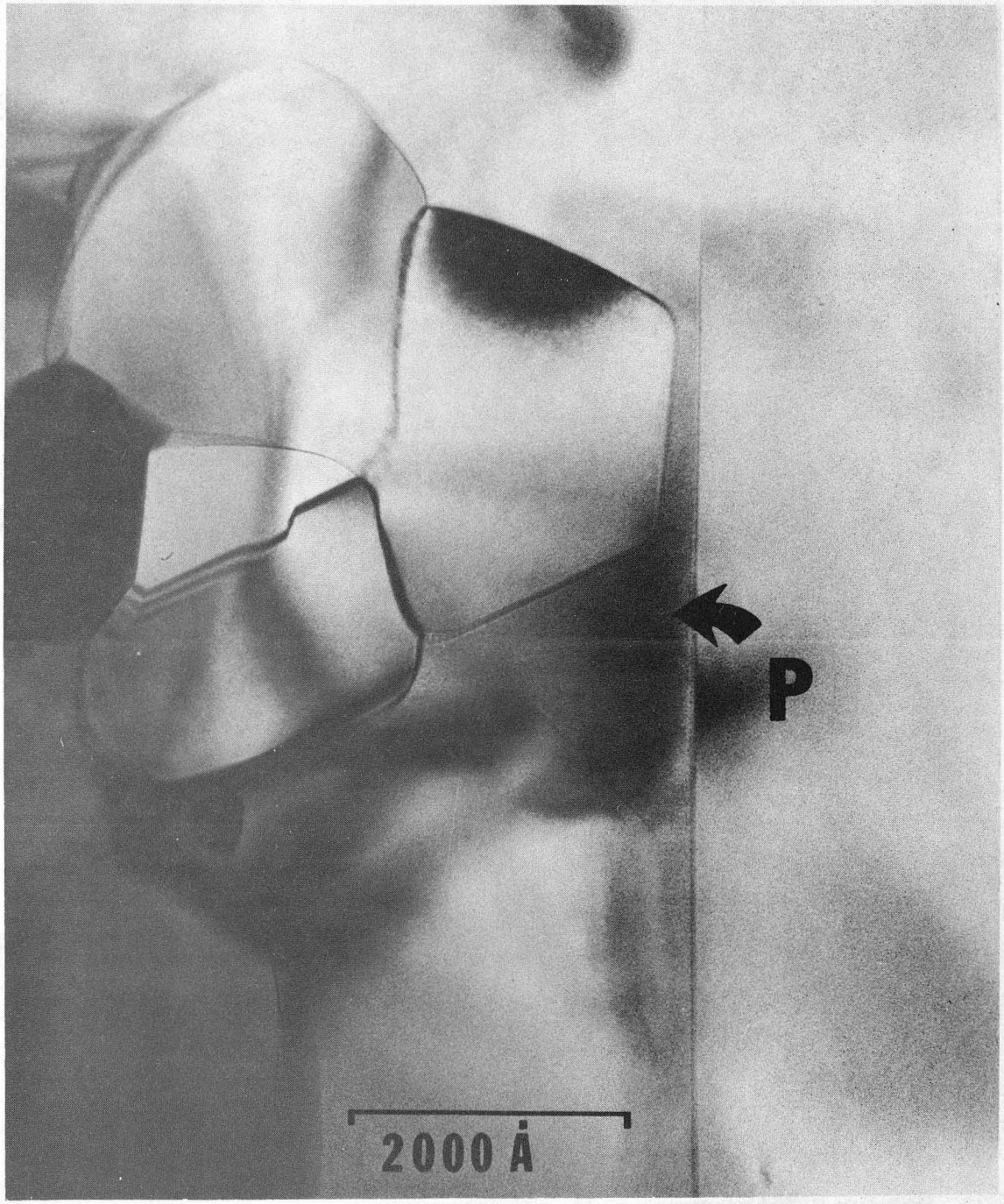

XBB 779-8604

Fig. 10

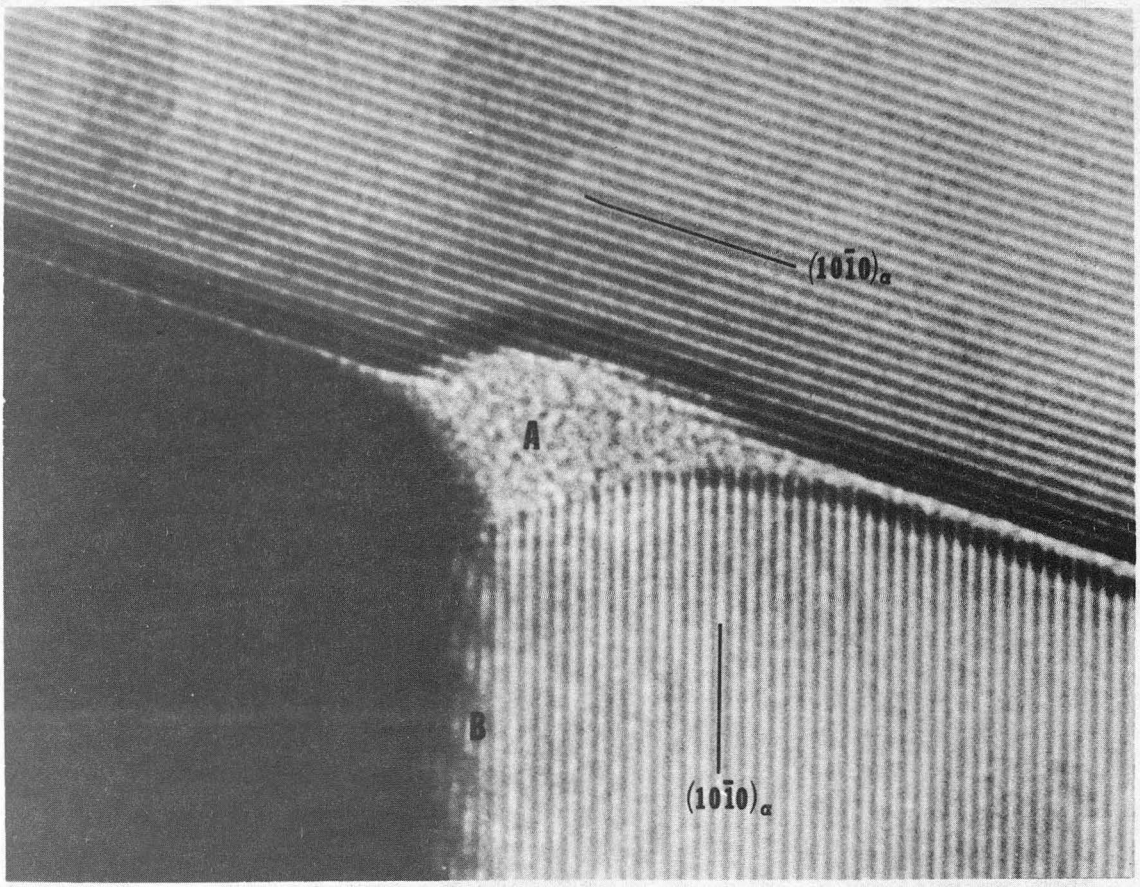

XBB 769-8516

Fig. 11

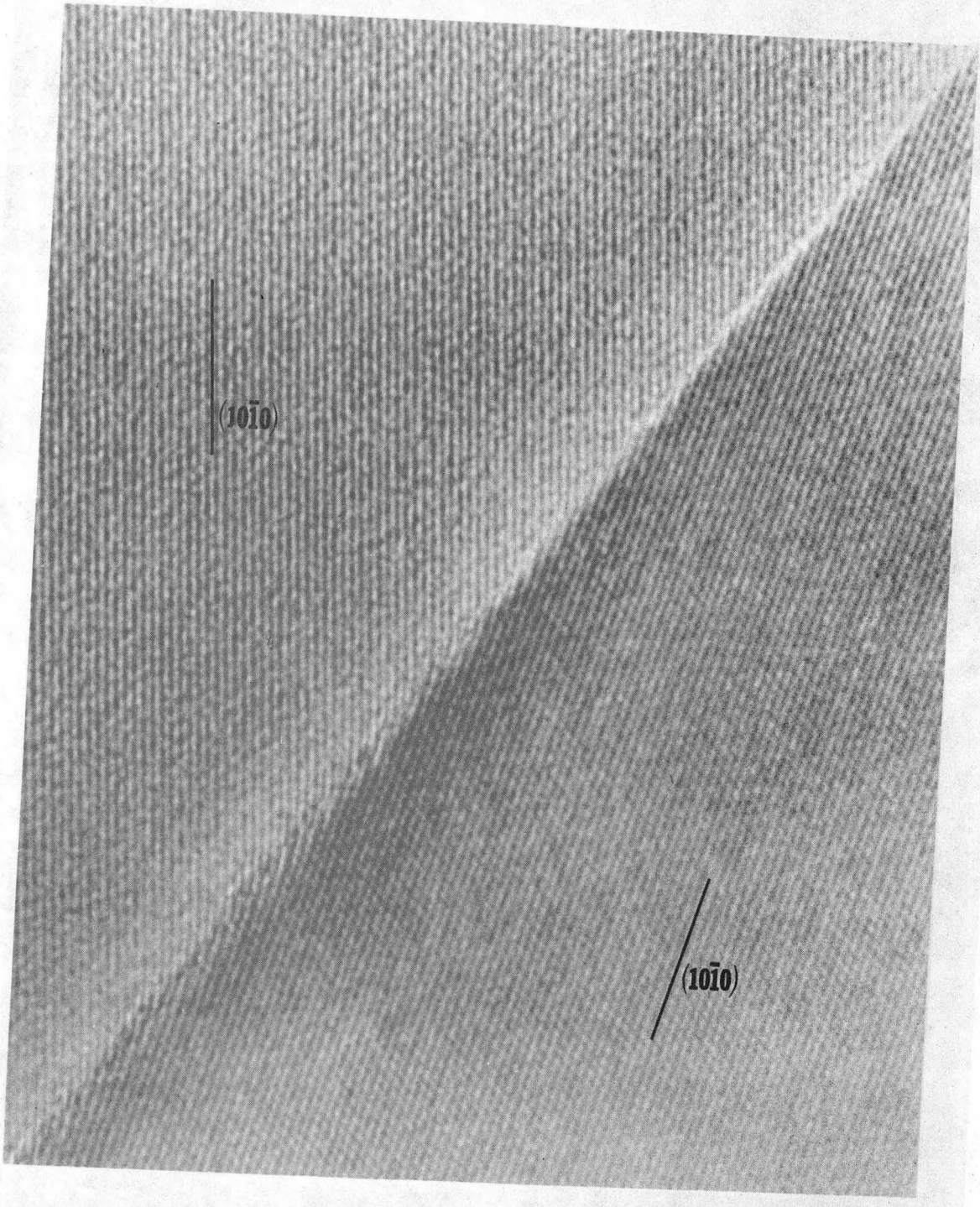

XBB 779-8609

Fig. 12

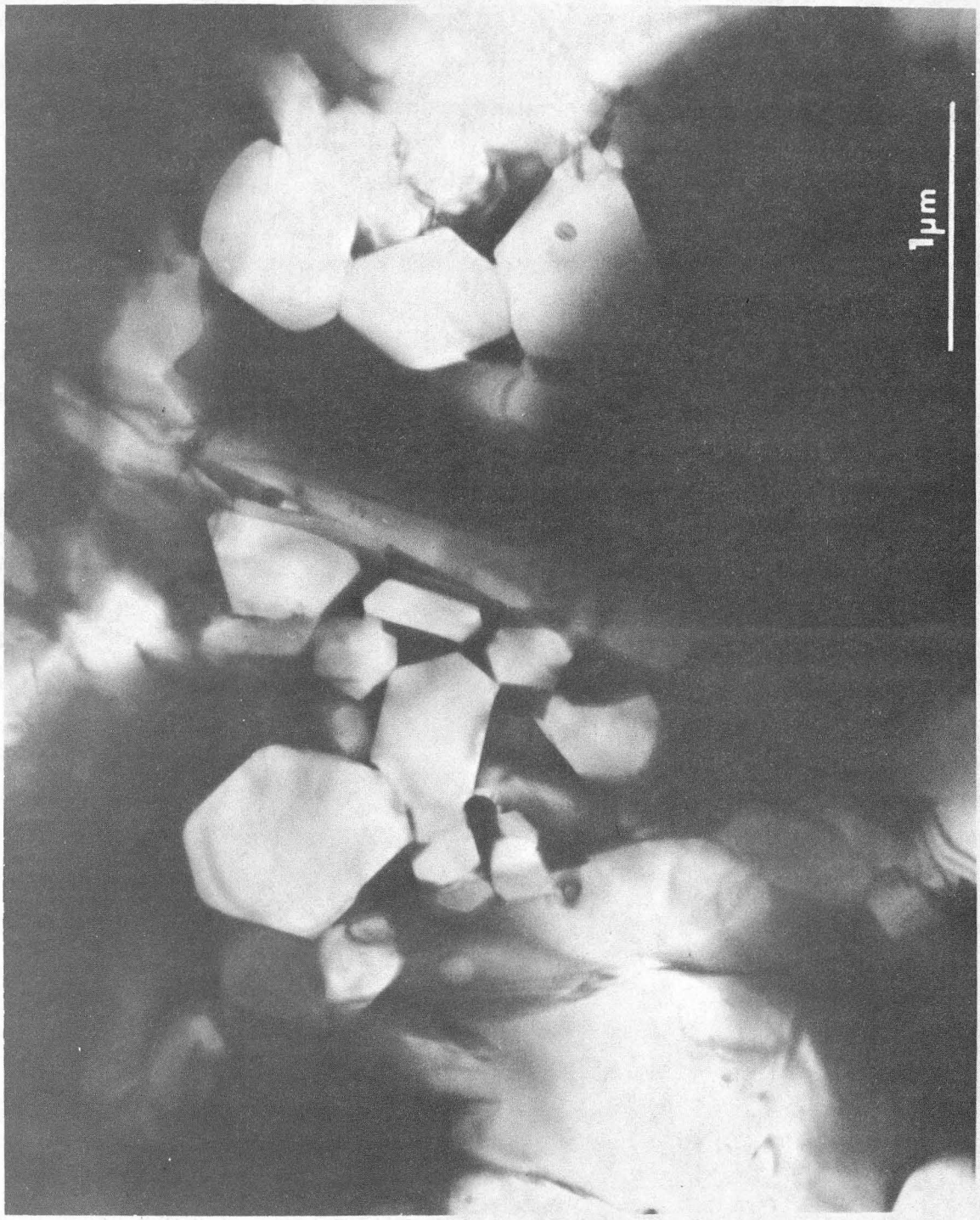

XBB 770-10387

Fig. 13

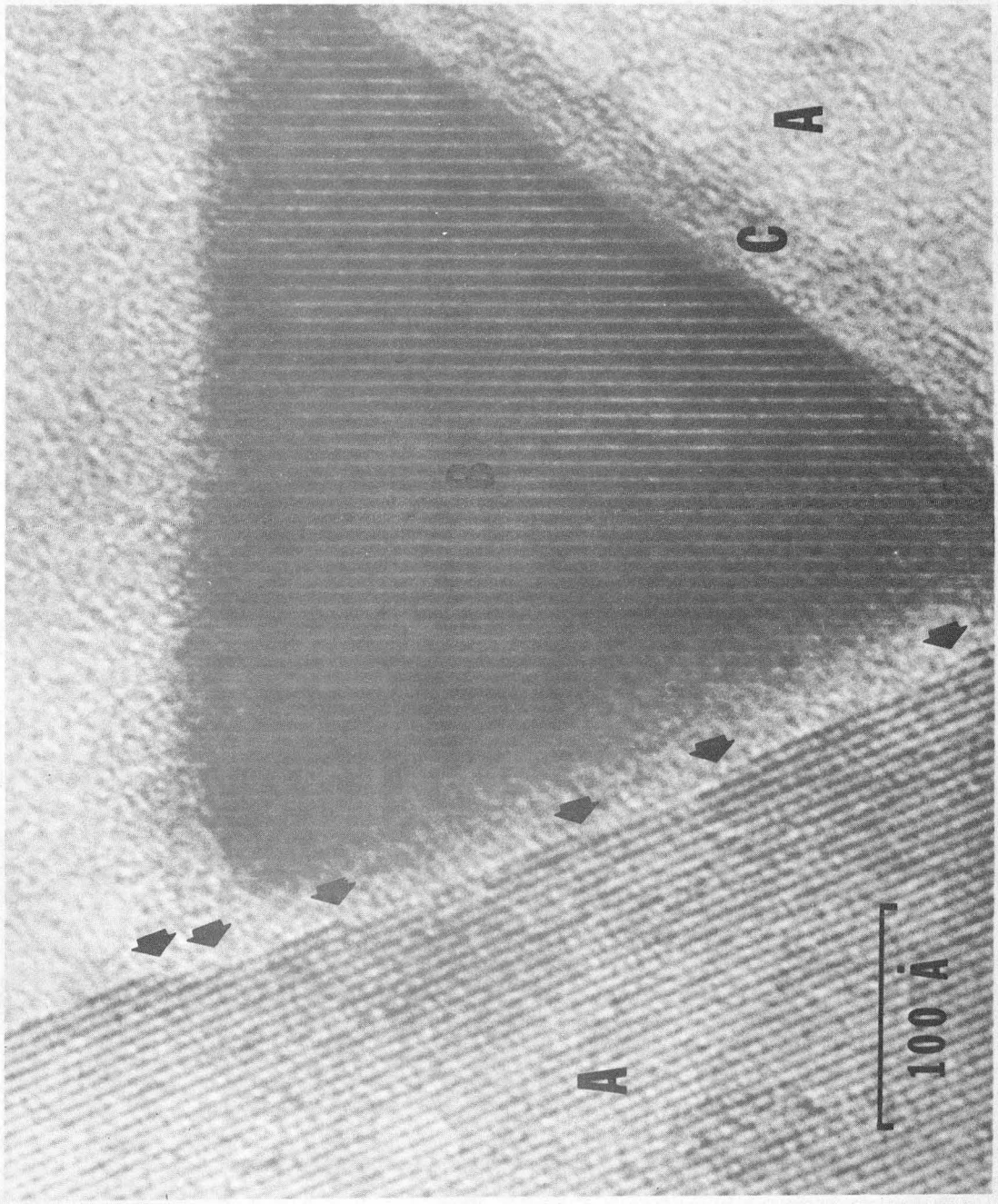

XBB 778-7367

Fig. 14

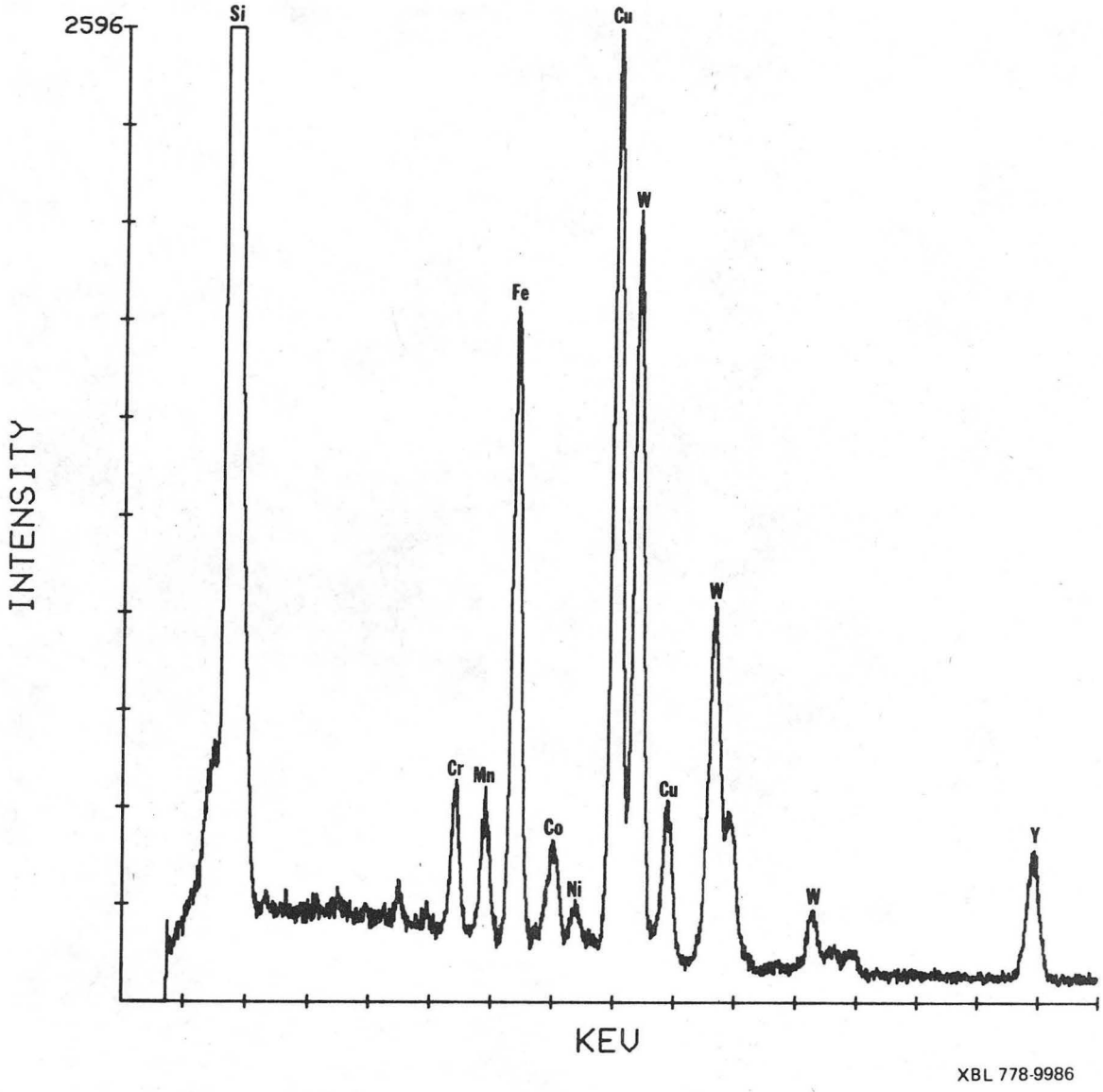

Fig. 15

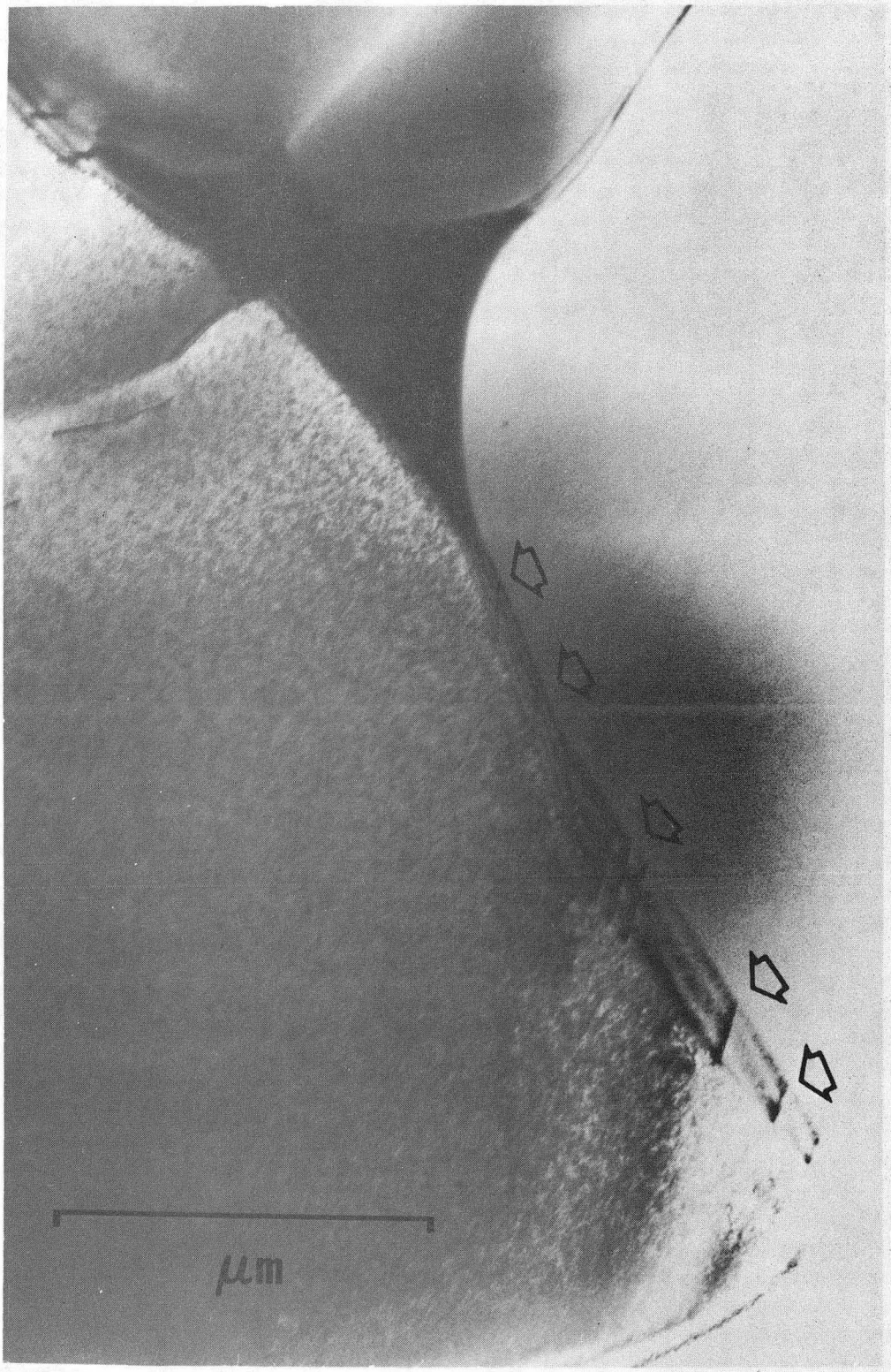

XBB 778-6949

Fig. 16

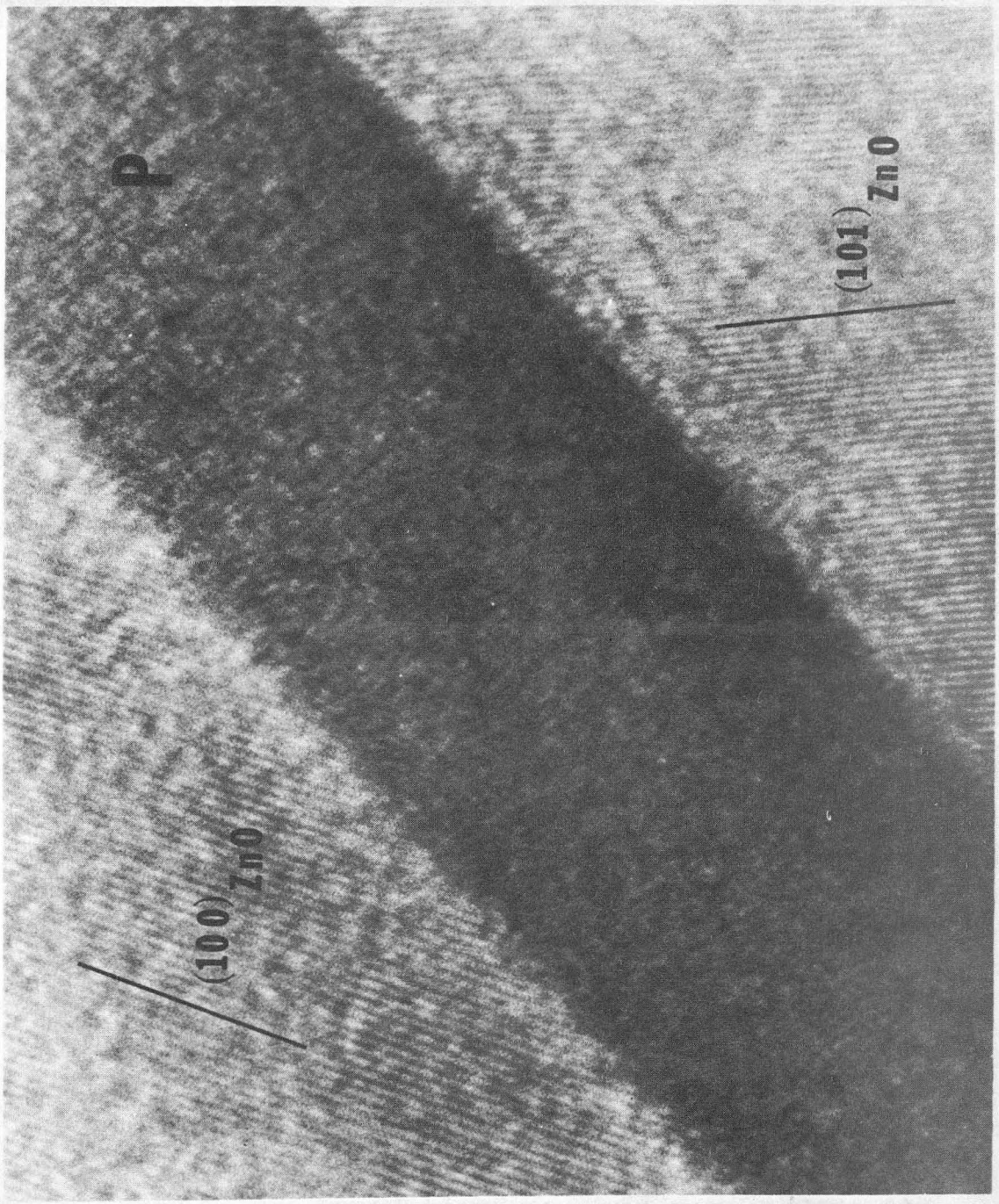

XBB 777-6377

Fig. 17

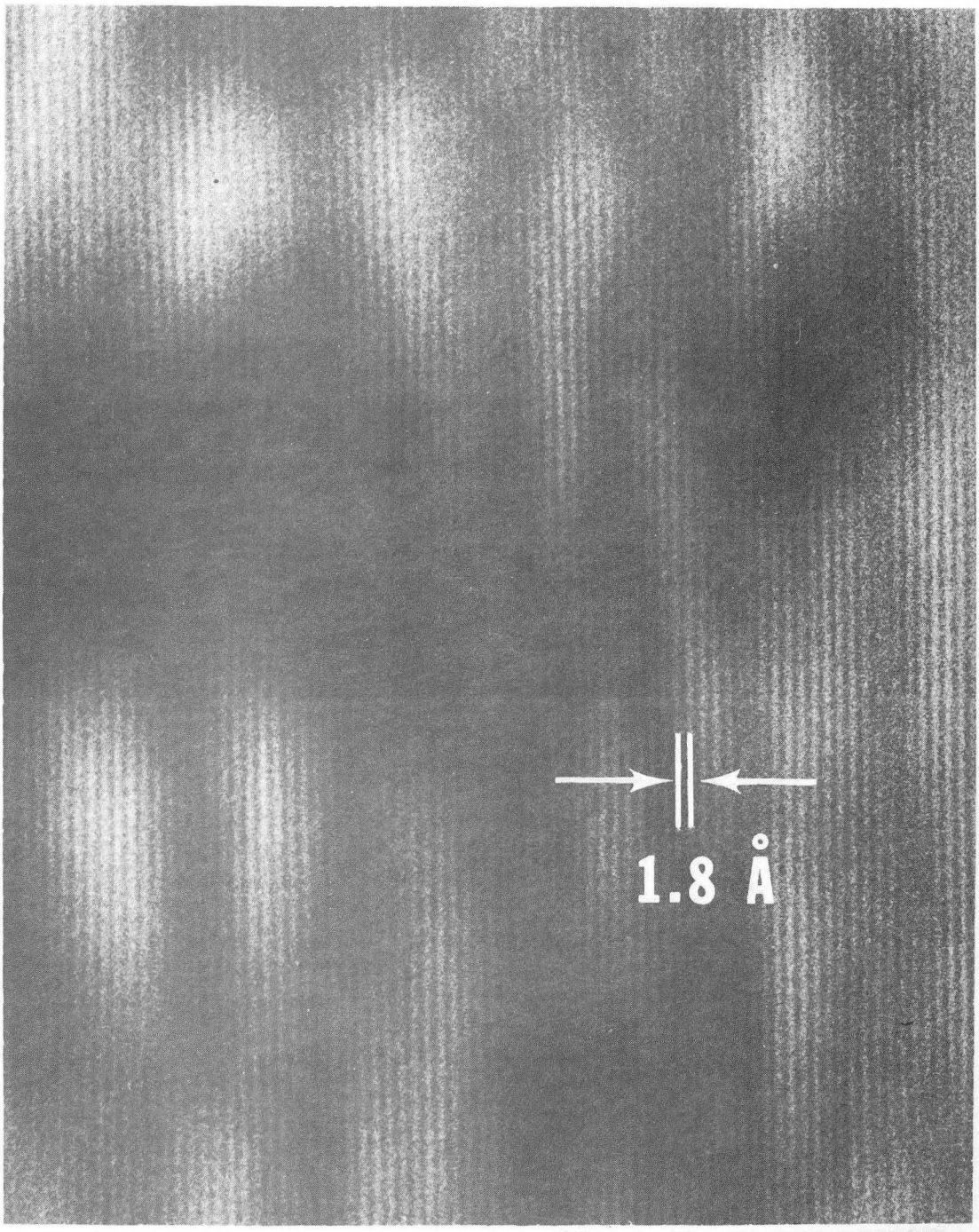

XBB 757-5130

Fig. 18

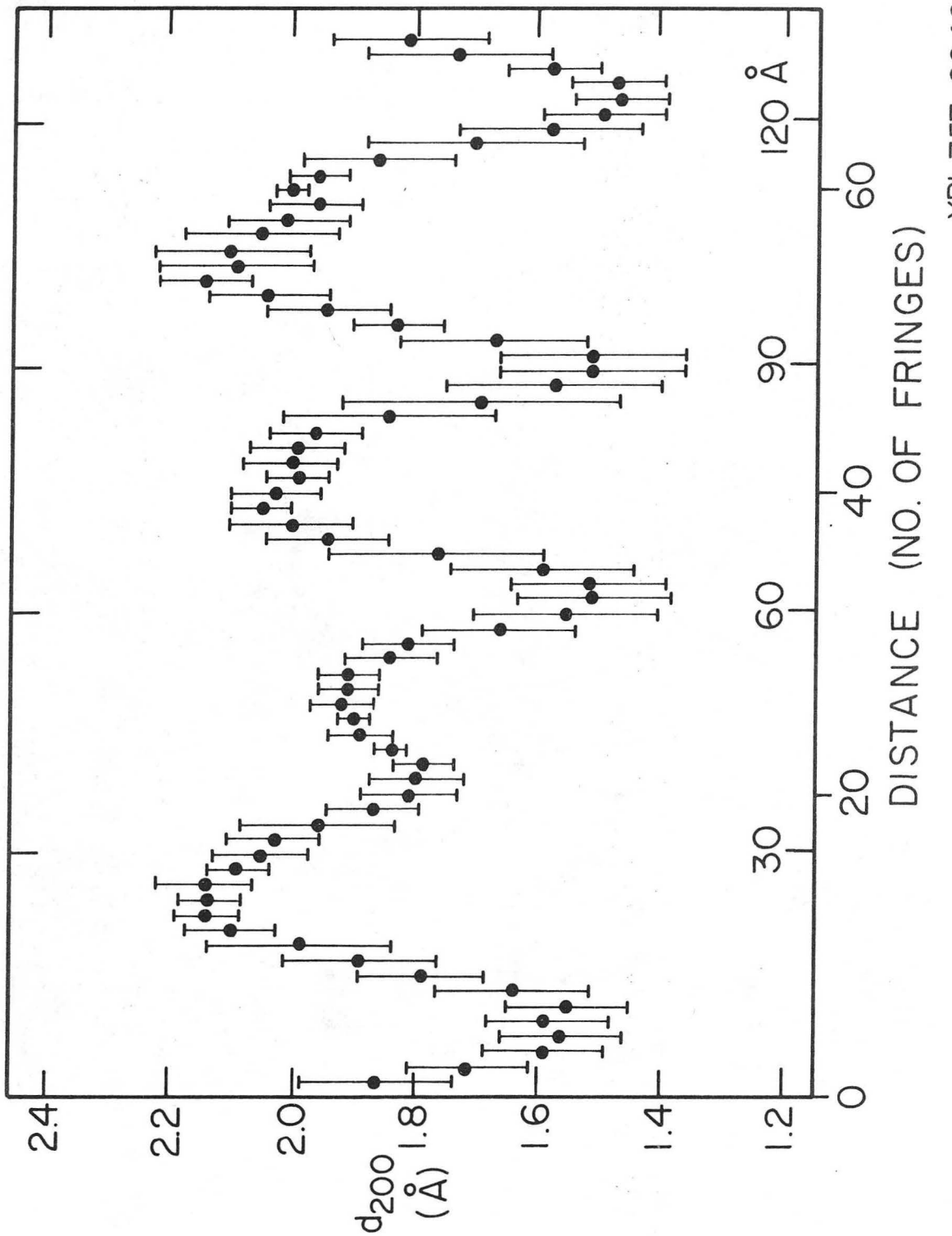

XBL 757-6648

Fig. 19

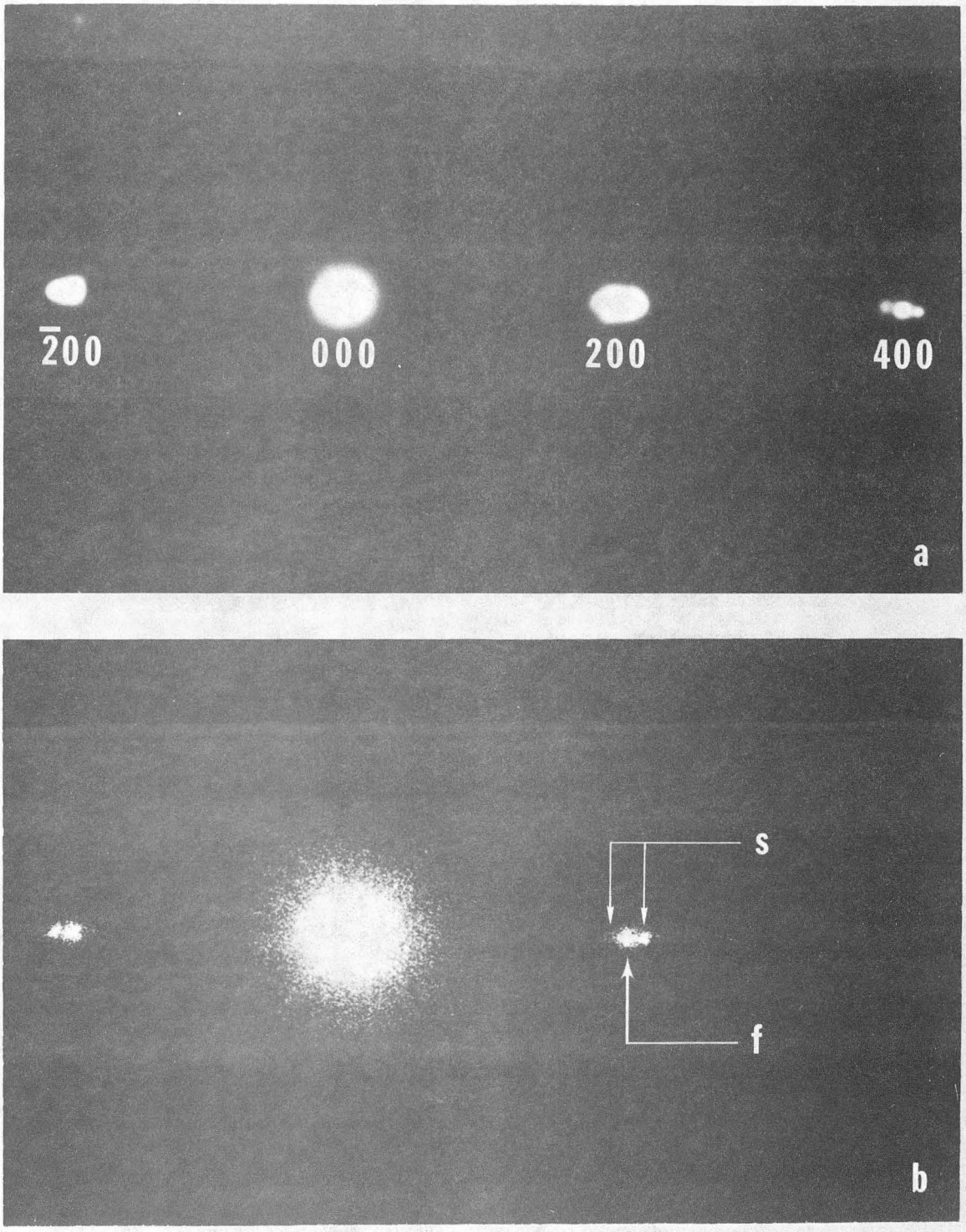

XBB 757-5132-A

Fig. 20

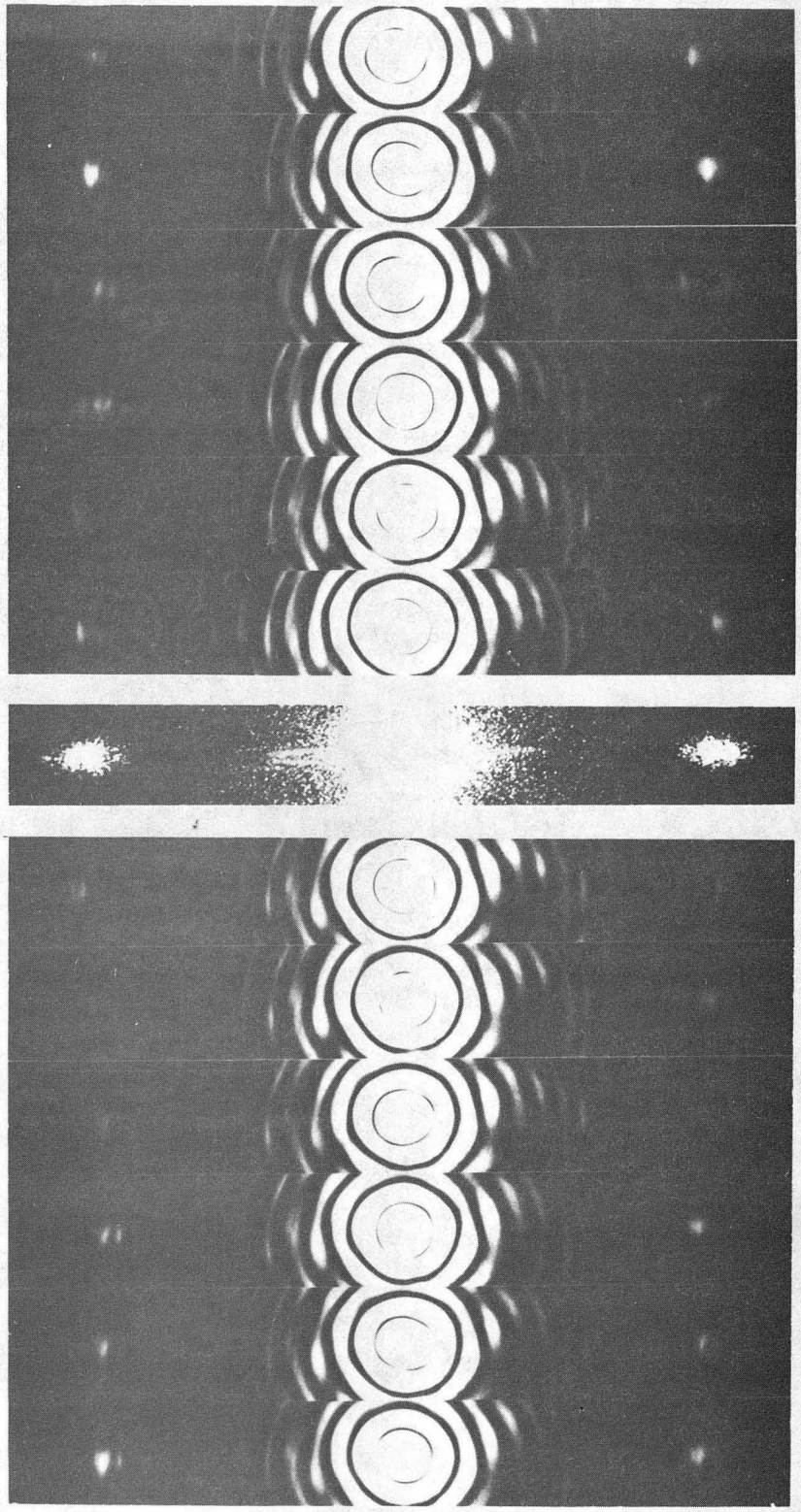

XBB 763-2668

Fig. 21

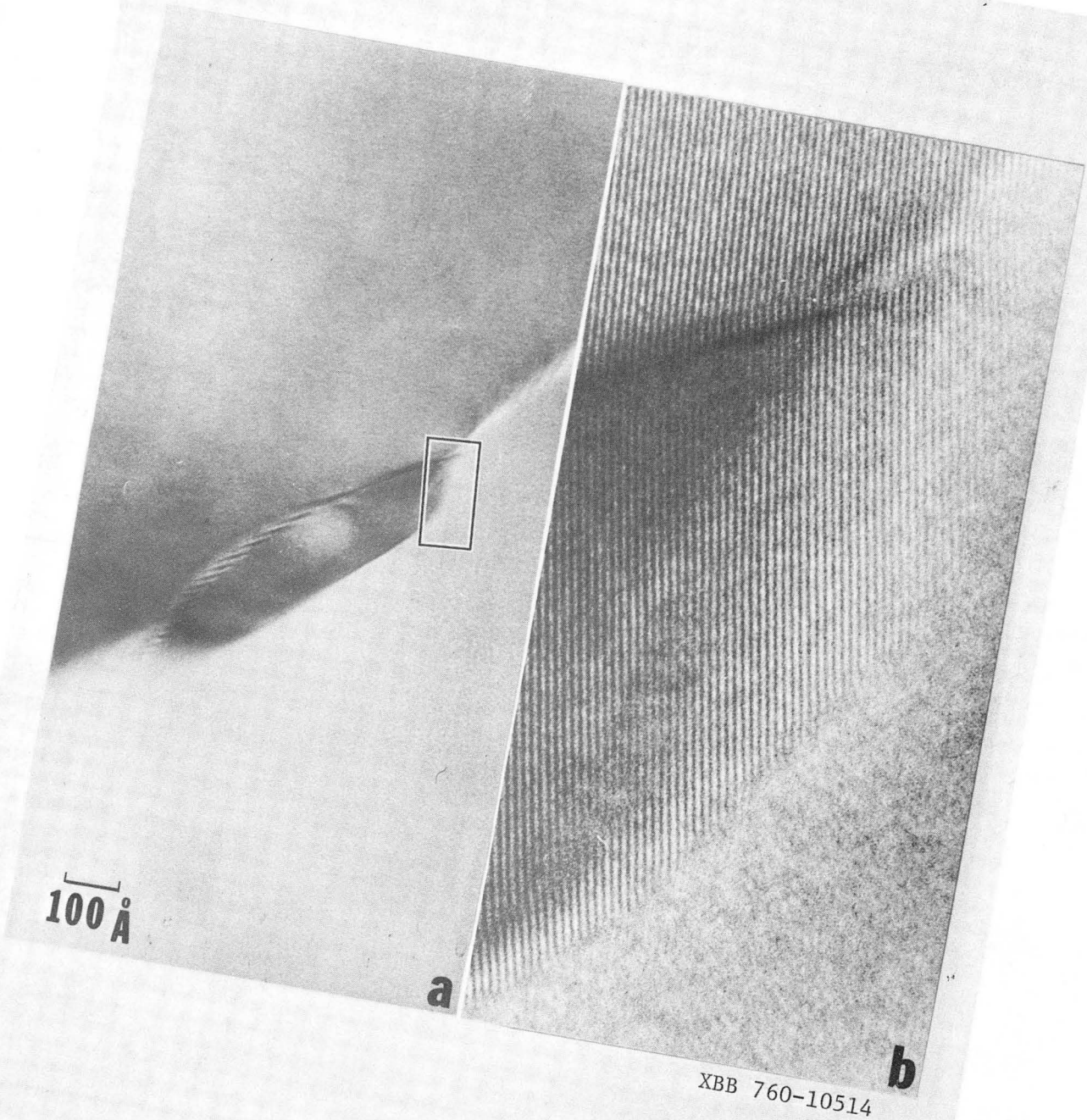

XBB 760-10514

Fig. 22

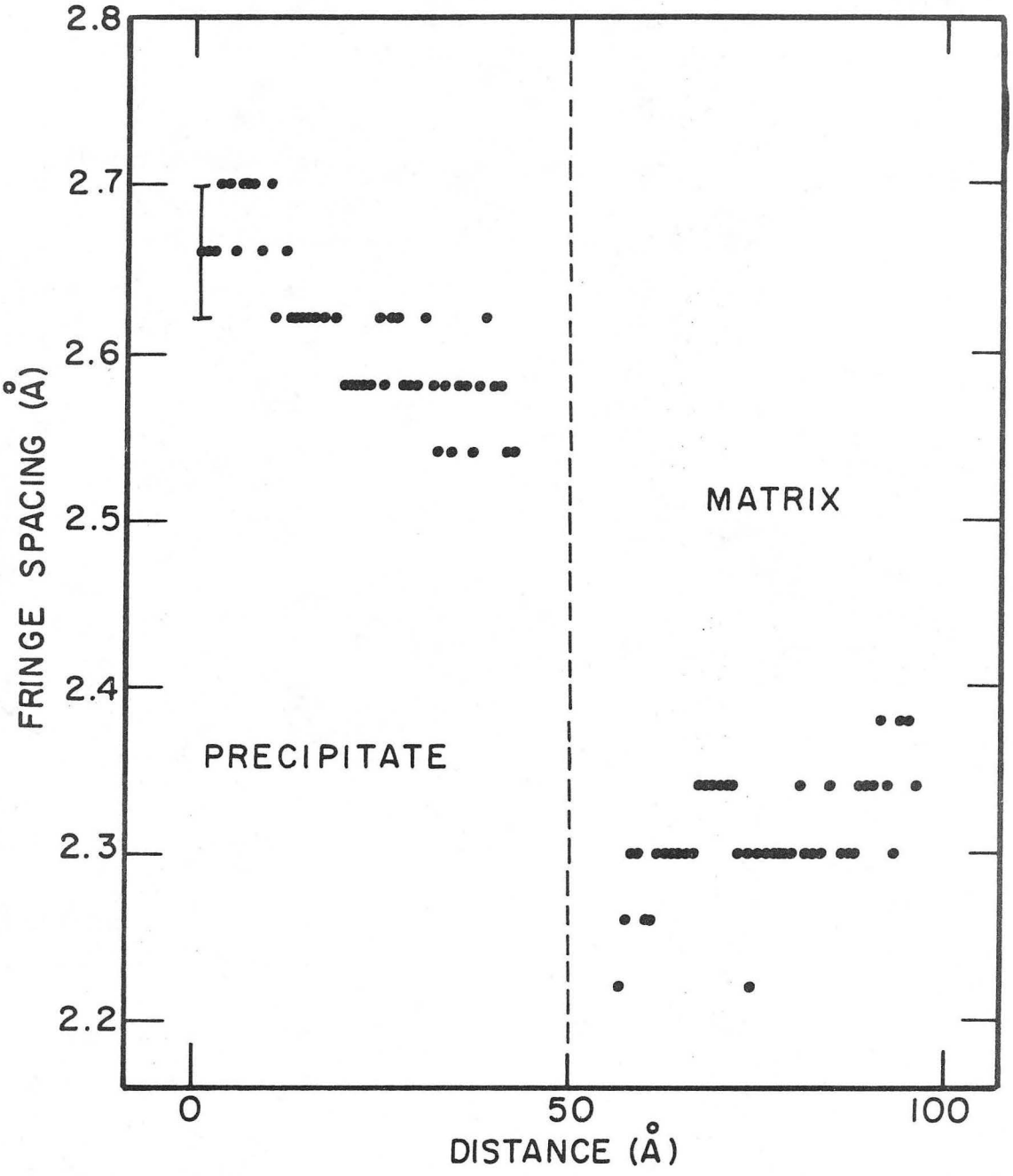
2.8
2.7
2.6
2.5
2.4
2.3
2.2
FRINGE SPACING (Å)
PRECIPITATE
MATRIX
0
50
100
DISTANCE (Å)
XBL 7611-7804

Fig. 23

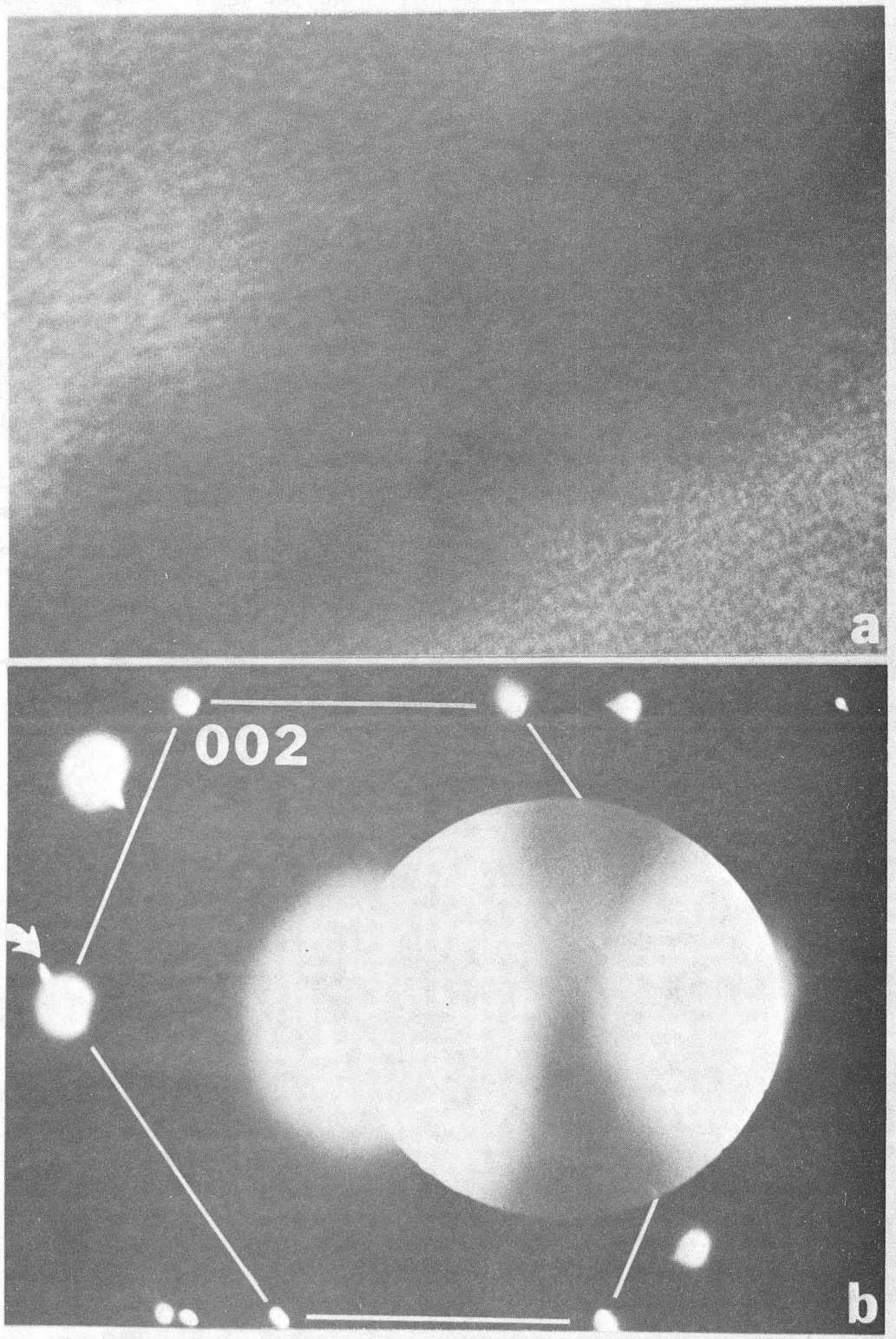

XBB 760-10525

Fig. 24

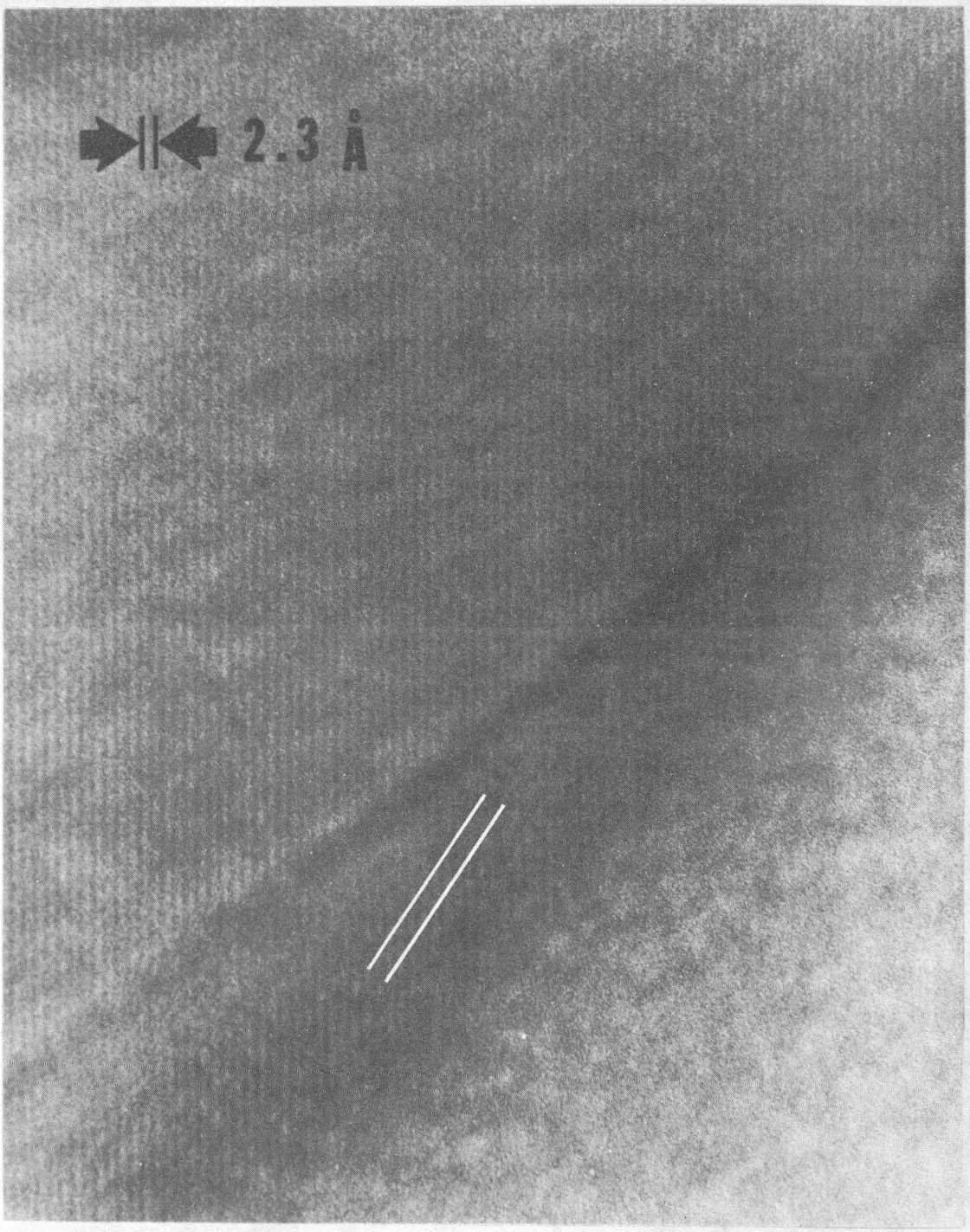

XBB 760-10515

Fig. 25

This report was done with support from the Department of Energy. Any conclusions or opinions expressed in this report represent solely those of the author(s) and not necessarily those of The Regents of the University of California, the Lawrence Berkeley Laboratory or the Department of Energy.

TECHNICAL INFORMATION DEPARTMENT
LAWRENCE BERKELEY LABORATORY
UNIVERSITY OF CALIFORNIA
BERKELEY, CALIFORNIA 94720